

Photolytically Induced Changes in Composition and Volatility of Biogenic Secondary Organic Aerosol from Nitrate Radical Oxidation during Night-to-day Transition

Cheng Wu¹, David M. Bell^{2*}, Emelie L. Graham¹, Sophie Haslett¹, Ilona Riipinen¹, Urs Baltensperger²,
5 Amelie Bertrand², Stamatios Giannoukos^{2,a}, Janne Schoonbaert², Imad El Haddad², Andre S. H. Prevot²,
Wei Huang³, Claudia Mohr^{1*}

¹Department of Environmental Science, Stockholm University, Sweden

²Laboratory of Atmospheric Chemistry, Paul Scherrer Institute, Villigen, Switzerland

³Institute for Atmospheric and Earth System Research / Physics, Faculty of Science, University of Helsinki, Helsinki, 00014,
10 Finland

^aNow at: Department of Chemistry and Applied Biosciences, ETH Zurich, Switzerland

Correspondence to: David M. Bell (david.bell@psi.ch) and Claudia Mohr (claudia.mohr@aces.su.se)

Abstract. Night-time reactions of biogenic volatile organic compounds (BVOCs) and nitrate radicals (NO₃) can lead to the formation of secondary organic aerosol (BSOA_{NO3}). Here we study the impacts of light exposure on the chemical composition and volatility of BSOA_{NO3} formed in the dark from three precursors (isoprene, α -pinene, and β -caryophyllene) in atmospheric simulation chamber experiments. Our study represents BSOA_{NO3} formation conditions where reactions between peroxy radicals (RO₂ + RO₂) and between RO₂ and NO₃ are favored. The emphasis here is on the identification of particle-phase organonitrates (ONs) formed in the dark and their changes during photolytic aging on timescales of \sim 1 h. Chemical composition of particle-phase compounds was measured with a chemical ionization mass spectrometer with filter inlet for gases and aerosols (FIGAERO-CIMS) and an extractive electrospray ionisation time-of-flight mass spectrometer (EESI-TOF). Volatility information of BSOA_{NO3} was derived from FIGAERO-CIMS desorption profiles (thermograms) and a volatility tandem differential mobility analyser (VTDMA). During photolytic aging, there was a relatively small change in mass due to evaporation (< 5 % for the isoprene and α -pinene BSOA_{NO3}, 12 % for the β -caryophyllene BSOA_{NO3}), but we observed significant changes in the chemical composition of the BSOA_{NO3}. Overall, 4853 %, 445 %, and 6062 % of the total signal mass for the isoprene, α -pinene, and β -caryophyllene BSOA_{NO3} was sensitive to photolytic aging and exhibited decay. The photolabile compounds include both monomers and oligomers. Oligomers can decompose into their monomer units through photolysis of the bonds (e.g. likely O-O) between them. Fragmentation of both oligomers and monomers also happened at other positions, causing the formation of compounds with shorter carbon skeletons. The cleavage of the nitrate functional group from the carbon chain was likely not a main degradation pathway in our experiments. In addition, photolytic degradation of compounds changes their volatility, and can lead to evaporation. We used different methods to assess bulk volatilities and discuss their changes during both dark aging and photolysis in context of the chemical changes we observed. We also reveal

large uncertainties in saturation vapor pressure estimated from parameterization for the ON oligomers with multiple nitrate groups. Overall, our results suggest that photolysis causes photodegradation of a substantial fraction of BSOA_{NO₃}, changes both the chemical composition and the bulk volatility of the particles, and might be a potentially important loss pathway of BSOA_{NO₃} during the night-to-day transition.

1 Introduction

Secondary organic aerosol (SOA), formed via the oxidation of volatile organic compounds (VOCs) emitted from human activities (anthropogenic) and vegetation (biogenic), has important impacts on climate (Shrivastava et al., 2017) and human health (Daellenbach et al., 2020). Biogenic VOCs such as isoprene (C₅H₈), monoterpenes (C₁₀H₁₆) and sesquiterpenes (C₁₅H₂₄), are key precursors for global SOA formation due to their larger emissions (Guenther et al., 2006; Guenther et al., 1995) and higher reactivity towards atmospheric oxidants compared to the VOCs from anthropogenic emissions. While oxidation initiated by ozone (O₃) and hydroxyl radicals (OH) dominates during daytime, nitrate radicals (NO₃), generated at night by the reaction of nitrogen dioxide (NO₂) with O₃, are the major nocturnal oxidant. Modeling studies estimate that 5–21 % of SOA are produced globally by NO₃ chemistry (Hoyle et al., 2007; Pye et al., 2010).

The reaction of NO₃ with VOCs is a major pathway for the production of organonitrates (ONs, RONO₂), which represent a substantial fraction of submicron aerosol nitrate at both urban and rural sites (Kiendler-Scharr et al., 2016). ONs also play an important role in the removal and transport of nitrogen oxides (NO_x), and impact NO_x cycling and O₃ formation (Perring et al., 2013). While the lifetime of aerosols in the atmosphere typically spans over multiple day/night cycles, the lifetime of ONs within the particles is much shorter (Lee et al., 2016; Zare et al., 2018). Reactions influencing particulate lifetime of ONs include oxidation, hydrolysis (Pye et al., 2015; Takeuchi and Ng, 2019), and photolysis (Müller et al., 2014; Suarez-Bertoa et al., 2012). They change both chemical and physical properties of SOA and ONs, and have different impacts on the atmospheric NO_x budget.

Compared to OH and O₃, there are few laboratory studies on NO₃-initiated biogenic SOA (BSOA_{NO₃}). Very little is known about the chemical composition and volatility of BSOA_{NO₃}. While there are extensive studies on photolytic/photochemical (photolysis + OH) aging of OH- and O₃- initiated SOA under low NO_x conditions (Surratt et al., 2006; Walser et al., 2007; Mang et al., 2008; Pan et al., 2009; Henry and Donahue, 2012; Presto et al., 2005; Zawadowicz et al., 2020), studies on photolytic/photochemical aging of NO₃-initiated SOA and ONs are limited. The few studies that have examined optical properties of SOA show that there is a significant difference in SOA produced from NO₃ oxidation compared to other oxidation pathways (Nakayama et al., 2015; Peng et al., 2018), as well as in BSOA_{NO₃} from different precursors (He et al., 2021). Nah et al. (2016) reported that SOA from β-pinene + NO₃ is generally resilient to photochemical aging and does not exhibit significant changes in its chemical composition, while most of the SOA from α-pinene + NO₃ evaporates during photochemical aging (photolysis + OH). However, little is known about SOA from other VOC precursors, and formed in chemical regimes

with different branching ratios for the peroxy radical (RO₂) pathways such as RO₂ + HO₂, RO₂ + NO₃ and RO₂ + RO₂. The knowledge gaps related to the effects of photolysis on lifetime and physicochemical properties of ONs currently hinders a quantitative understanding of their impacts on the atmospheric nitrogen budget, chemical interactions between anthropogenic and biogenic compounds, and climate.

In this study, we performed chamber experiments of dark formation and photolytic aging of NO₃-initiated SOA and ONs from three biogenic VOCs, namely isoprene (C₅H₈), α-pinene (C₁₀H₁₆), and β-caryophyllene (C₁₅H₂₄). This article is a companion paper to “Particle-phase processing of α-pinene NO₃ secondary organic aerosol in the dark”, published in the same journal (Bell et al., 2021)(Bell et al., 2021). Bell et al. (2021) Bell et al. (2021) present the evolution of the composition of NO₃-initiated SOA from α-pinene during dark aging. Here, we focus on the impacts of photolytic aging on both the chemical composition and volatility of BSOA_{NO3}. We compare the chemical composition of particle-phase compounds before and after 1 h of ultraviolet (UV) irradiation using advanced mass spectrometric techniques, determine photolabile fractions for each BSOA_{NO3} system, and investigate the potential chromophores that photolyze. In addition, we also examine the changes in the bulk volatility with both parameterization and experimental methods.

2 EXPERIMENTAL SECTION

2.1 Chamber and experimental description

Experiments were conducted in the Paul Scherrer Institute (PSI) Simulation Chamber for Atmospheric Chemistry (PSI-SCAC, (Platt et al., 2013)), which is an 8 m³ flexible Teflon chamber suspended in a temperature-controlled shipping container. The chamber is surrounded by a bank of black lights (40 x 100 W Cleo Performance solarium lamps, Philips (Krapf et al., 2016)). The experiments were performed under humid conditions (RH ≈ 60 %) and at a temperature of 21 ± 3 °C (with an increase of 3–4 °C during photolysis). A list of the experiments is given in Table 1.

Table 1 List of experiments and summary of experimental conditions

Exp.	Precursor	VOC reacted (ppb)	N ₂ O ₅ (ppb)	Max OA loading (μg m ⁻³)	SOA yield (%)
1	Isoprene	100	180–220	24	9
2	Isoprene	100	100–120	11	4
3	α-Pinene	100	300	18	3
4	β-Caryophyllene	50	200+	464	110

SOA was formed in the chamber by the reaction of the precursors with NO₃ radicals. Each experiment followed a similar protocol. First, the chamber was cooled from 30 °C to ~20 °C, then humidity was increased by boiling MilliQ water (18 M-Ohm) until the desired RH was reached. After the chamber conditions were stabilized, the desired VOC was injected into the chamber volumetrically, and its concentration was monitored with a proton transfer reaction mass spectrometer (Quadrupole PTR-MS, Ionicon). β-Caryophyllene could not be monitored with the PTR-MS because its mass-to-charge (*m/z*) ratio of 204

Th is outside of the mass transmission range for quantitative measurements, though trace amounts of the molecule were detected in the experiment. After the VOC concentration had been stable for 5–15 min, N₂O₅ was injected into the chamber, which acted as the source of NO₃ radicals via decomposition. N₂O₅ was synthesized by reacting O₃ (~1–2 %, with an Innovatec ozone generator using PSI-provided O₂) with a pure source of NO₂ (99 %). N₂O₅ crystals were collected by passing the gaseous components into a cooled flask (-70 °C). Each day the sample was brought to the chamber in a dry-ice ethanol bath and warmed for 1–2 min prior to injection (5 L min⁻¹ for ~10 s). A 0-d box model (F0AM) (Wolfe et al., 2016) utilizing the Master Chemical Mechanism (MCM) (Jenkin et al., 1997) was used to model the VOC precursor decay to determine a range of initial N₂O₅ concentrations. This was performed when the VOC was measurable, which was not the case for the β-caryophyllene experiments (Exp. 4), where the estimate of 200+ ppb (Table 1) comes from the average N₂O₅ concentrations in the other experiments performed. After the injection was complete, the chamber was stirred by injecting zero air into the chamber (100 L min⁻¹ for ~10 min). Following chamber stirring, the volume of the chamber started to decrease due to all of the instruments sampling air from the chamber. Experiments started under dark conditions to probe NO₃-initiated SOA formation, and to follow its chemical transformation with no external stimulus. After ~3–5 h of dark aging, the chamber was irradiated with UV lights ($\lambda_{\text{Max}} = 350 \text{ nm}$, see Platt et al. (2013)) for about 1 h to test the impacts of photolytic aging. After each experiment, ~1000 ppb O₃ was added, the chamber was continuously flushed with zero air (~100 L min⁻¹), and the temperature of the enclosure was increased to 30 °C overnight to promote the evaporation of HNO₃ from the walls of the chamber.

O₃ was measured with an O₃ analyzer (Thermo 49C), NO_x and NO₂ with a chemiluminescence NO_x monitor (Thermo 42C). Aerosol number size distributions were measured by a scanning mobility particle sizer (SMPS, TSI model 3938). Both a chemical ionization mass spectrometer with filter inlet for gases and aerosols (FIGAERO-CIMS, Aerodyne Research, Inc.) with iodide as the reagent ion, and an extractive electrospray ionization time-of-flight mass spectrometer (EESI-TOF, ToFwerk) were used to measure the molecular composition of organic compounds. The FIGAERO-CIMS performed semi-continuous online measurements and shifted analysis between the particle phase and the gas phase, and the EESI-TOF continuously measured the particle phase with rapid response. In a subset of the experiments (Exp. 1, Exp. 2 and Exp. 4), the evaporation of particles was measured with a custom-built volatility tandem differential mobility analyser (VTDMA) (Tritscher et al., 2011).

2.2 Chemical ionization mass spectrometer with filter inlet for gases and aerosols

The design and operation of the FIGAERO-CIMS were similar to those described in previous studies (Lopez-Hilfiker et al., 2014; Lee et al., 2014; Huang et al., 2018). In this study, the FIGAERO inlet was coupled to a high-resolution time-of-flight chemical-ionization mass spectrometer (HR-ToF-CIMS) ($M/\Delta M \sim 5,000\text{--}6,000$), and I⁻ was used as reagent ion. An X-ray generator was used to ionize methyl iodide and produce the reagent ion in a nitrogen flow. Particles were collected on a 25mm Zefluor® PTFE filter (Pall Corp.) inside the FIGAERO via a sampling port (stainless steel tube of ca. 1.5 m length, flow rate 5 L min⁻¹). The duration of particle-phase sampling depended on the mass concentrations in the chamber and was 10–20 min for most of the experiments. For each experiment, three to four filters were sampled during dark aging, and one filter was

collected after about 1 h of photolytic aging. In addition, one particle blank was performed for each experiment during dark
aging (details about background subtraction see Fig. S1 and the supporting information (SI)). During particle-phase collection,
gases were measured via a 6 mm Teflon tube of ~1 m length at 5 L min⁻¹. When the particle-phase sampling was completed,
the gas-phase measurement was switched off and particles on the filter were desorbed by a flow of ultra-high-purity (99.999
%) nitrogen. A FIGAERO desorption round lasted about 55 min: 20 min of ramping the temperature of the nitrogen flow from
ambient temperature up to 200 °C were followed by a 20 min “soak period” at a constant temperature of 200 °C, and 15 min
of cooling down to room temperature. The mass spectral signal evolutions as a function of desorption temperature are termed
thermograms (Lopez-Hilfiker et al., 2014). The integration of thermograms of individual compounds (cooling period excluded)
yields their total signal in counts per deposition. Here we did not convert the counts per deposition into chamber concentrations,
as we only show normalized signal (either signal normalized to the dominating compound or to the sum signal of all
compounds). We observed modest or negligible fragmentation due to thermal desorption in the FIGAERO inlet (5–27 %, 1–4
%, 10–23 % of the total organic signal of the isoprene, α -pinene and β -caryophyllene SOA, respectively). As shown in Fig. S3, m
Most of the thermograms of the individual compounds for all systems exhibited unimodal and sharp peaks. Thermal
fragmentation products were detected either through thermograms of individual compounds with multiple peaks (normally
double peaks) or one peak with T_{\max} (desorption temperature at which a compound’s signal exhibits a maximum) much higher
than the estimated T_{\max} (e.g., for α -pinene SOA, a C₁₀ monomer had a $T_{\max} \approx 140$ °C which is in the range of T_{\max} for C₂₀
dimers (Faxon et al., 2018)). Artefacts resulting from thermal fragmentation products were corrected for (see the SI S1.2 and
Fig. S2). In addition, only a small fraction (< 1 % of the total mass) of the compounds were deprotonated. In this study, we
only report the molecules clustered with I. Further information concerning the correction of thermal decomposition and the
data analysis is provided in the SI.

2.3 Extractive electrospray ionization time-of-flight mass spectrometer

A detailed description of the EESI-TOF can be found in previous work (Lopez-Hilfiker et al., 2019; Pospisilova et al., 2020)
and the companion paper (Bell et al., 2021) (Bell et al., 2021). In brief, the EESI-TOF samples the aerosol formed in the
chamber via a sampling line (~3.5 m long stainless steel) and removes the gaseous components by passing the sampled volume
through a multi-channel charcoal denuder. The aerosol sample then intersects a spray of droplets emanating from a fused silica
electrospray capillary (50:50 H₂O:acetonitrile doped with 100 ppm NaI). The droplets envelope the aerosol sample and extract
the water soluble fraction of the aerosol. During droplet evaporation a majority of the extracted molecules bind to Na⁺, creating
positively charged adducts. The ions are guided to the time-of-flight mass spectrometer ($M/\Delta M \sim 5,500\text{--}7,000$) where their
mass-to-charge ratio is determined. Background measurements were conducted every 4 minutes for 1 minute by passing the
sample air through a particle filter. The reported signal throughout the work are the difference spectra of consecutive 4-minute
average signal and 1-minute average background signal. The EESI-TOF signal (Hz) is scaled by the molecular weight of each
molecular ion in order to represent the EESI-TOF signal as a mass-based measurement (ag s⁻¹). Artefacts associated with these
measurements are discussed in the companion paper associated with this publication (Bell et al., 2021) (Bell et al., 2021). The

EESI-TOF data for most experiments had similar bulk sensitivities, except for the α -pinene experiment (Exp. 3), which was about a factor of 10 lower because the EESI-TOF was still being optimized, and capillary position and TOF settings were being altered.

160 2.4 Volatility tandem differential mobility analyser

The custom-built VTDMA (see e.g. Tritscher et al. (2011)) sampled aerosols through the same inlet as the EESI-TOF and the SMPS, and a silica gel diffusion drier downstream from the chamber. The VTDMA combines two differential mobility particle sizer (DMPS) systems, coupled in series with a heating unit in between. Both DMPS systems consist of a custom made DMA (Stockholm University, operated with closed-loop sheath air) and a condensation particle counter (CPC, TSI 3010). Before entering each DMPS system the particles were brought into charge equilibrium using a Ni-63 source. The first DMA selected a nearly monodisperse aerosol with the diameter set to the geometric mean diameter measured in situ by the SMPS upstream (122127, 8784, and 21908 nm during both dark aging and photolysis for Exp. 1, Exp. 2 and Exp. 4, respectively). The sample flow was then split into two, with one half going to the CPC measuring the selected particle concentration and the other half entering a 35 cm long custom-built thermodenuder (TD) with a residence time of 1.9 s, which heated the aerosol to 150 °C in Exp. 1 and Exp. 2 and 175 °C in Exp. 4. The size distribution (over 15 bins) of the heated aerosol was measured in the second DMPS system with a time resolution of approximately 5 min, and the change in size was converted to an estimate of the volume fraction remaining (VFR):

$$\text{VFR} = \frac{D(T)^3}{D_{\text{init}}^3} \quad (\text{Eq. 1})$$

where D_{init} is the initial diameter, and $D(T)$ are the heated (Temperature T) diameters, represented by the geometric mean mode diameter estimated using a Gaussian fit of the whole heated size distribution.

2.5 Wall loss correction

The particle mass concentrations (in $\mu\text{g m}^{-3}$) were derived from integrated number size distributions and their conversions to mass using an assumed organic aerosol density (1.19 g cm^{-3} (Vaden et al., 2011)). They were corrected for wall losses using a uniform dynamic wall loss rate k_{wall} for the whole size range. k_{wall} was determined from the observed exponential decay of the particle number concentration (taking coagulation into account) using Eq. 2, where N corresponds to the particle number concentration and k_{coag} corresponds to the coagulation coefficient ($5 \cdot 10^{-10} \text{ s}^{-1}$ (Pospisilova et al., 2020)).

$$\frac{dN}{dt} = -k_{\text{coag}} * N^2 - k_{\text{wall}} * N \quad (\text{Eq. 2})$$

The wall loss-corrected particle mass concentration was divided by the uncorrected mass concentration to obtain the wall loss correction factor applied to the EESI-TOF and FIGAERO-CIMS signal. In the experiments performed here, the total number concentration (in cm^{-3}) varied between 10^6 and 10^4 at the beginning of the experiment to 10^4 and 10^3 at the end of the experiment. In experiments with large number concentrations (e.g. $> 5 \cdot 10^4 \text{ cm}^{-3}$, in Exp. 4), coagulation was a dominant particle sink, which resulted in a mobility diameter that increased during the experiment, even though the mass was decreasing

from evaporation. The particle number concentration was constrained to be constant throughout the lifetime in the chamber, based upon k_{wall} and k_{coag} . Evaporation of semi-volatile compounds will not affect the particle wall loss correction because this does not change the particle number concentration, only the particle volume (or mass).

2.6 Estimating bulk saturation mass concentration C^* based on FIGAERO-CIMS and VTDMA

The saturation mass concentration (C^*) of individual compounds was calculated based on their molecular composition using three different previously published parameterizations:

1) an updated version of the parameterization by Donahue et al., 2011, modified based on the saturation concentrations of highly oxygenated molecules (HOMs) detected by Tröstl et al. (2016) and published by Mohr et al. (2019):

$$\log_{10} C^* = (n_{\text{O}} - n_{\text{C}})b_{\text{C}} - (n_{\text{O}} - 3n_{\text{N}})b_{\text{O}} - 2 \frac{n_{\text{C}}(n_{\text{O}} - 3n_{\text{N}})}{n_{\text{C}} + n_{\text{O}} - 3n_{\text{N}}} b_{\text{CO}} - n_{\text{N}}b_{\text{N}} \quad (\text{Eq. 3})$$

where $n_{\text{O}} = 25$, $b_{\text{C}} = 0.475$, $b_{\text{O}} = 0.2$, $b_{\text{CO}} = 0.9$ and $b_{\text{N}} = 2.5$. n_{C} , n_{O} and n_{N} are number of carbon, oxygen and nitrogen atoms in the compound, respectively. For ONs, it is assumed that a nitrate group reduces a compound's vapor pressure by about 2.5 orders of magnitude (Donahue et al., 2011; Pankow and Asher, 2008).

2) an updated version of Li et al. (2016) with modified nitrogen coefficient for organic nitrates (Isaacman-VanWertz and Aumont, 2021):

$$\log_{10} C^* = (n_{\text{O}} - n_{\text{C}})b_{\text{C}} - n_{\text{O}}b_{\text{O}} - 2 \frac{n_{\text{C}}n_{\text{O}}}{n_{\text{C}} + n_{\text{O}}} b_{\text{CO}} - n_{\text{N}}b_{\text{N}} \quad (\text{Eq. 4})$$

where $n_{\text{O}} = 22.66$, $b_{\text{C}} = 0.4481$, $b_{\text{O}} = 1.656$, $b_{\text{CO}} = -0.7790$ for CHO compounds, and $n_{\text{O}} = 24.13$, $b_{\text{C}} = 0.3667$, $b_{\text{O}} = 0.7732$, $b_{\text{CO}} = -0.07790$ and $b_{\text{N}} = -1.5464$ for CHON compounds. n_{C} , n_{O} and n_{N} are number of carbon, oxygen and nitrogen atoms in the compound, respectively. The modification of the parameterization is based on the observation that a nitrate group has a similar impact on vapor pressure as a hydroxyl, thus one nitrate group (one nitrogen atom and three oxygen atoms) reduces a compound's vapor pressure by 0.7732 orders of magnitude (Isaacman-VanWertz and Aumont, 2021).

3) a parameterization based on highly oxygenated organic molecules (HOMs) from α -pinene ozonolysis (Peräkylä et al. (2020)):

$$\log_{10} C^* = 0.18 \times n_{\text{C}} - 0.14 \times n_{\text{H}} - 0.38 \times n_{\text{O}} + 0.80 \times n_{\text{N}} + 3.1 \quad (\text{Eq. 5})$$

where n_{C} , n_{H} , n_{O} and n_{N} are number of carbon, hydrogen, oxygen and nitrogen atoms in the compound, respectively. With this parameterization, a nitrate group reduces a compound's vapour pressure by 0.34 orders of magnitude.

We note here that more such parametrizations exist in literature (Donahue et al., 2011; Daumit et al., 2013). We choose these three parameterizations as they have explicit formulations for nitrate groups/nitrogen. The parametrizations calculate C^* at a temperature of 300 K. The temperature dependence of C^* is considered as follows:

$$C^*(T) = C^*(300 \text{ K}) \exp\left(\frac{\Delta H^{\text{VAP}}}{R} \left(\frac{1}{300 \text{ K}} - \frac{1}{T}\right)\right) \quad (\text{Eq. 6})$$

where T is the temperature in Kelvin, $C^*(300 \text{ K})$ is the saturation concentration at 300 K, R is the gas constant, and ΔH^{VAP} is the vaporization enthalpy:

$$\Delta H^{\text{VAP}} = -11 \log_{10} C^*(300 \text{ K}) + 129 ; \Delta H^{\text{VAP}} < 200 \text{ kJ/mol} \quad (\text{Epstein et al., 2010}) \quad (\text{Eq. 7})$$

220 For each filter sample from the FIGAERO-CIMS, the mass-weighted average $\log_{10} C^*$ for the entire particle population deposited on the filter (bulk) was calculated and adjusted to the same T (298.3 K) as that used by the kinetic model (see the description below) for further comparison.

The T_{max} , the desorption temperature at which a compound's signal exhibits a maximum in the FIGAERO-CIMS, has earlier been shown to be connected qualitatively to the compound's volatility ($\log_{10} C^*$ or enthalpy of vaporization) (Lopez-Hilfiker
225 et al., 2014; Thornton et al., 2020; Bannan et al., 2019). For each filter sample from the FIGAERO-CIMS, we calculated the mass-weighted average T_{max} of the entire particle population deposited on the filter (bulk).

As an additional method to constrain the bulk volatility, VTDMA measurements of the VFR were used to determine the bulk $\log_{10} C^*$ with a kinetic model that simulates the evaporation of a monodisperse aerosol in the heated part of the VTDMA (Riipinen et al., 2010). The bulk $\log_{10} C^*$ (at 298.3 K) was determined manually so that the calculated VFR matches the
230 measurements. Additional model input parameters include the settings of the VTDMA, i.e. initial particle diameter and concentration, together with the residence time and temperature in the heated section and the ambient temperature at the time of the measurement.

3 RESULTS AND DISCUSSION

3.1 Mass yields of isoprene, α -pinene and β -caryophyllene $\text{BSOAN}_{\text{O}_3}$

235 As shown in Table 1, the wall loss-corrected SOA yields and maximal mass concentrations formed from isoprene, α -pinene, and β -caryophyllene are 4–9 % at 11–24 $\mu\text{g m}^{-3}$, 3 % at 18 $\mu\text{g m}^{-3}$ and 110 % at 464 $\mu\text{g m}^{-3}$, respectively. The SOA yields observed here are comparable to previously reported values: For isoprene + NO_3 , yields between 2 % and 24 % have been presented (Rollins et al., 2009; Ng et al., 2008); for α -pinene + NO_3 , between 0 % and 16 % (Hallquist et al., 2009; Nah et al., 2016; Fry et al., 2014); and for β -caryophyllene + NO_3 , between 86 % and 146 % (Fry et al., 2014; Jaoui et al., 2013). The
240 yields at the lower end of the range of reported values of the isoprene and α -pinene SOA in our study can likely be explained by the lack of seed aerosol in those experiments. For β -caryophyllene, most of the products are of sufficiently low volatility (see section 3.5) and the SOA yields are similar to those from the seeded experiments. The variation in SOA yields can also be caused by different chemical regimes, resulting e.g. in different branching ratios for the peroxy radicals (RO_2) + hydroperoxyl radical (HO_2), $\text{RO}_2 + \text{NO}_3$ and $\text{RO}_2 + \text{RO}_2$ pathways after the initial RO_2 formation via $\text{NO}_3 + \text{VOCs}$. The $\text{RO}_2 + \text{RO}_2$ pathway is a more effective channel for forming SOA than the $\text{RO}_2 + \text{HO}_2$ and $\text{RO}_2 + \text{NO}_3$ pathways (Ng et al., 2008). In Ng et al. (2008), the SOA yield from the isoprene + NO_3 experiments (seeded), where the $\text{RO}_2 + \text{RO}_2$ pathway dominated, was much higher (23.8 %) than that from experiments where the $\text{RO}_2 + \text{NO}_3$ pathway dominated (4.3 %), because $\text{RO}_2 + \text{RO}_2$ chemistry led to the formation of oligomers. In the study of Nah et al. (2016), the branching ratios for the $\text{RO}_2 + \text{HO}_2$, $\text{RO}_2 + \text{NO}_3$ and $\text{RO}_2 + \text{RO}_2$ pathways were 5:4:1, and a SOA yield of 1.7 % at 1.2 $\mu\text{g m}^{-3}$ (no seed) was observed for α -pinene + NO_3
245 SOA. In our experiments, we achieved higher SOA yields from α -pinene + NO_3 , due to N_2O_5 :VOC ratios between 1 and 5 and
250

the radical balance being dominated by either $\text{RO}_2 + \text{RO}_2$ (at low $\text{N}_2\text{O}_5:\text{VOC}$) or $\text{RO}_2 + \text{NO}_3$ (at high $\text{N}_2\text{O}_5:\text{VOC}$) chemistry and no significant source of HO_2 radicals. As discussed in Bell et al. (2021) [Bell et al. \(2021\)](#), even in experiments where the ratio of $\text{N}_2\text{O}_5:\text{VOC}$ is high (~ 3) and the $\text{RO}_2 + \text{NO}_3$ pathway is predicted by the MCM model to be dominant, the initial composition of $\text{BSOA}_{\text{NO}_3}$ formed here in the dark is still dominated by $\text{RO}_2 + \text{RO}_2$ reactions, resulting in substantial fractions of oligomers and indicating that the rate of the $\text{RO}_2 + \text{RO}_2$ pathway is likely underestimated by the MCM model.

The evolution of the SOA mass concentrations and particle size during both dark aging (2 h before photolysis) and photolysis are shown in Fig. 1 for all systems. Before photolysis, for the α -pinene system (Exp. 3), steady evaporation was observed from the particles, which is consistent with shrinking mean diameter (from 240 to 233 nm) resulting in 15 % loss of particle mass (wall-loss corrected) or volume. For the two isoprene experiments (Exp. 1 and Exp. 2), ~ 6 % of the mass was lost during dark aging. The wall-loss corrected mass concentrations of the β -caryophyllene SOA are stable throughout the dark aging period, while the geometric mean diameter of the particles increases from 229 nm (at time -2 h in Fig. 1) to 266 nm (at time 0 h), as a result of particle coagulation following the large number concentrations ($\sim 10^6 \text{ cm}^{-3}$). The differences in evaporation can likely be attributed to the lower volatility of β -caryophyllene monomers (C_{15}) compared to isoprene dimers (C_{10}) and α -pinene monomers (C_{10}) (for details see section 3.5). Overall, the $\text{BSOA}_{\text{NO}_3}$ formed during dark aging exhibits slight to moderate shrinkage of its mass and size (after wall loss-correction) after the initial production.

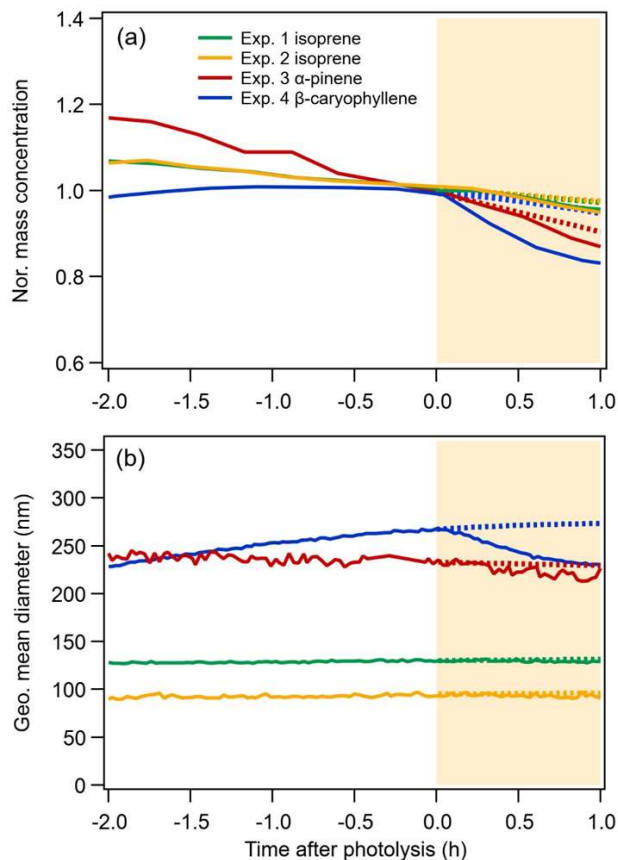
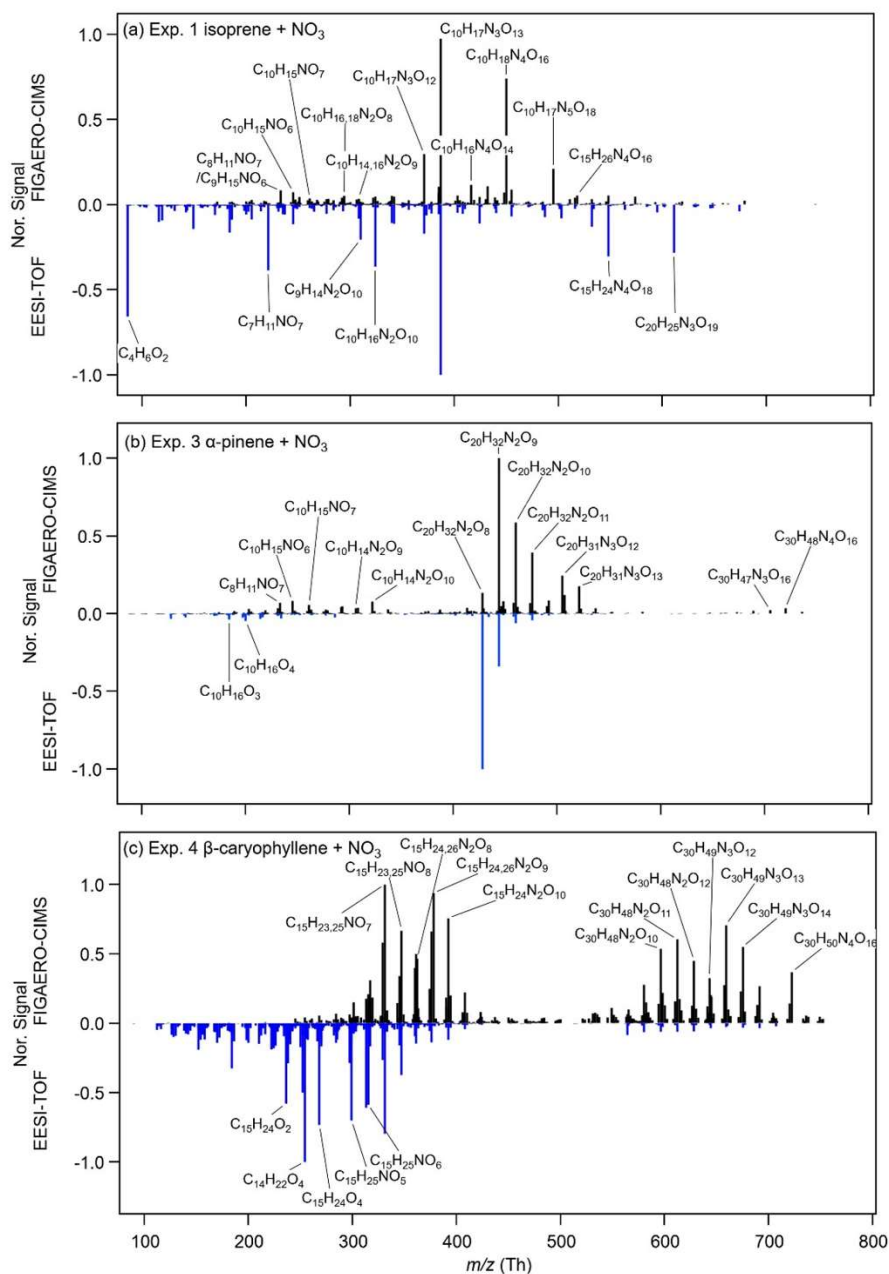


Fig. 1 Time series of normalized mass concentration (a) and geometric mean diameter (b) of the SOA measured by the SMPS. SOA mass loadings were corrected for particle wall losses based on the decay of the particle number concentration. The mass concentration is normalized to that when the lights were turned on. The area shaded in yellow corresponds to the period of UV irradiation. The expected curvature of the mass concentration and geometric mean diameter without UV irradiation is represented by the dashed lines.

3.2 Chemical composition of isoprene, α -pinene and β -caryophyllene BSOA_{NO₃}

In total, 478, 425, and 366 organic molecular compositions (including 436, 332, and 348 ONs) were identified with the FIGAERO-CIMS, and 359, 158, and 441 organic molecular compositions (including 273, 134, and 268 ONs) were identified with the EESI-TOF, for the isoprene, α -pinene and β -caryophyllene SOA, respectively. In the α -pinene + NO₃ experiment (Exp. 3), because of the lower sensitivity of the EESI-TOF compared to other experiments (described in 2.3), the detected compounds by the EESI-TOF were fewer than that detected in other experiments. Due to the dominating RO₂ + RO₂ pathway, oligomers make a substantial contribution to the total mass formed in the dark. The mass fractions of oligomers are ~100 %, 86–88 % and 60–63 % with the FIGAERO-CIMS and 97–98 %, 85–99 %, and 13–22 % with the EESI-TOF, for the isoprene, α -pinene and β -caryophyllene SOA, respectively. The dimer-to-monomer ratio varies across the three systems, and it increases with decreasing carbon number of the precursors.

The mass spectra of the particle-phase species of the three systems obtained from the FIGAERO-CIMS and the EESI-TOF shortly before switching on the lights are shown in Fig. 2. For the isoprene system, Exp. 1 and Exp.2 are similar, thus only Exp. 1 is presented here and Exp. 2 is presented in the SI (Fig. S5S6). For the isoprene SOA, monomers are negligible (C_{1-5} compounds are less likely to partition into the particle phase due to their relatively high volatility), and dimers with three to four nitrate groups (e.g. $C_{10}H_{17}N_3O_{13}$ and $C_{10}H_{18}N_4O_{16}$, each contributing 15 % to the total mass) dominate the mass measured by the FIGAERO-CIMS. Dimers with one, two and five nitrate groups, and trimers (C_{15}) also contribute a substantial fraction (65 %) to the total mass. The major compounds observed in our study are similar to those observed by Ng et al. (2008), who used a UPLC/(-)ESI-TOFMS and investigated ratios of N_2O_5 :isoprene from 0.6 to 5. For the EESI-TOF, the major compounds are similar, with the same highest peak ($C_{10}H_{17}N_3O_{13}$) as measured by the FIGAERO-CIMS. However, the relative intensities are different. Compared to the FIGAERO-CIMS, the EESI-TOF measures higher signals of $C_{10}H_{16}N_2O_{10}$, $C_{15}H_{24}N_4O_{18}$ and $C_{20}H_{25}N_3O_{19}$, but lower signals of $C_{10}H_{17}N_3O_{12}$, $C_{10}H_{18}N_4O_{16}$ and $C_{10}H_{17}N_5O_{18}$. There is a high signal from $C_4H_6O_2$, which comes from the degradation of oligomeric species $C_{10}H_{16}N_2O_{9,10}$ and $C_{10}H_{17}N_3O_{13,5}$. ~~to be discussed in a future paper (Bell et al., in preparation).~~



295

Fig. 2 FIGAERO-CIMS (positive axis) and EESI-TOF (negative axis) mass spectra of particle phase $\text{C}_x\text{H}_y\text{O}_z\text{N}_{0-4}$ formed during (a) Exp.1: isoprene + NO_3 , (b) Exp. 3: α -pinene + NO_3 and (c) Exp. 4: β -caryophyllene + NO_3 shortly before photolysis. For FIGAERO-CIMS, the last filter before photolysis is chosen (Pre 2 in the Fig. 3). The EESI-TOF mass spectra are averaged mass spectra during the same sampling time as that of FIGAERO-CIMS. All mass spectra are normalized to the corresponding maximal signal.

300 The α -pinene system according to the FIGAERO-CIMS measurements is dominated by C_{20} dimers with two nitrate groups, i.e. $C_{20}H_{32}N_2O_{8-13}$ make up 39 % of the total mass, while the monomers and trimers contribute 12–14 % and 3.7–4.4 %, respectively. Our mass spectra are similar to those reported in Takeuchi and Ng (2019) measured with a FIGAERO-CIMS, where the α -pinene + NO_3 SOA was dominated by C_{20} dimers with two dominating compounds, $C_{20}H_{32}N_2O_9$ and $C_{20}H_{32}N_2O_{10}$. The dominating monomer in their study was $C_{10}H_{15}NO_6$, also identical to our study. Their ratio of $C_{20}H_{32}N_2O_9$ to $C_{10}H_{15}NO_6$ was about 5, in our study ~ 2 times higher (about 10). In Takeuchi and Ng (2019), reactions between peroxy radicals ($RO_2 + RO_2$) and $RO_2 + NO_3$ are also favoured. Large concentrations of RO_2 present in both studies likely lead to the large fraction of oligomers. ~~Our mass spectra are similar to those reported in Takeuchi and Ng (2019) measured with a FIGAERO-CIMS, where the α -pinene + NO_3 SOA (N_2O_5 : α -pinene ~ 7) was dominated by C_{20} dimers with two dominating compounds, $C_{20}H_{32}N_2O_9$ and $C_{20}H_{32}N_2O_{10}$.~~ The EESI-TOF detected similar dimers and monomers as those measured by the FIGAERO-CIMS. However, 305
310 the highest peak measured is $C_{20}H_{32}N_2O_9$ for the FIGAERO-CIMS and $C_{20}H_{32}N_2O_8$ for the EESI-TOF. It is also worth noting that the EESI-TOF measured a few CHO compounds without nitrate groups, such as $C_{10}H_{16}O_3$ and $C_{10}H_{16}O_{4,5}$, ~~which may also stem from some degradation pathways in the EESI-TOF source.~~

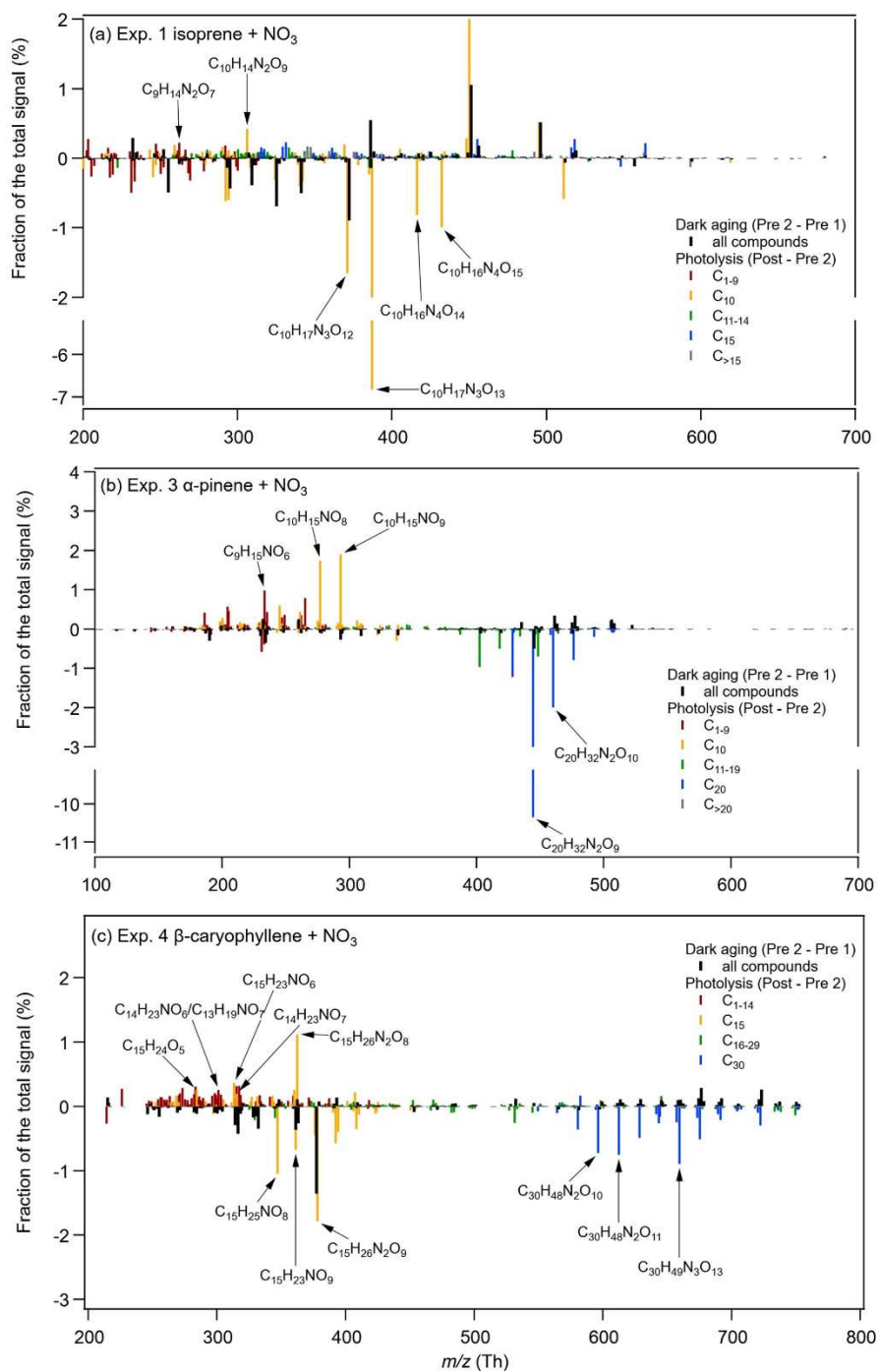
The β -caryophyllene SOA mass spectrum from the FIGAERO-CIMS is dominated by C_{15} monomers with 1–2 nitrate groups ($C_{15}H_{23,25}NO_{7,8}$ and $C_{15}H_{24,26}N_2O_{8-10}$) and C_{30} dimers with 2–3 nitrate groups ($C_{30}H_{48}N_2O_{10-12}$ and $C_{30}H_{49}N_3O_{12-14}$). The mass 315 spectrum from the EESI-TOF is dominated by C_{15} monomers with zero and one nitrate group. The contribution from the dimers is substantially smaller compared to FIGAERO-CIMS, which may result from a decreased sensitivity of larger m/z components as observed previously (Lopez-Hilfiker et al., 2019) and/or from decomposition of ON dimers. The higher contribution from the monomers, compared to the isoprene and α -pinene systems, is likely due to the larger number of carbon atoms of β -caryophyllene, and the two double bonds (one more than α -pinene), which both lead to low volatility of the monomers (for 320 details see section 3.5).

Overall, both instruments are able to cover the major compounds from both monomer and dimer regions, although the sensitivity towards different compounds varies. The I⁻ CIMS is not sensitive towards non-oxygenated compounds, monoalcohols, monoketones or monoaldehydes (Lee et al., 2014), while the EESI-TOF is sensitive to nearly all compounds present in SOA but not sensitive to non-oxygenated compounds (Lopez-Hilfiker et al., 2019). ~~Some Differences~~ are may also 325 ~~be~~ caused by the fragmentation of oligomers into smaller compounds ($C_xH_yO_2C_xH_yO_2$) insidewith the EESI-TOF, such as $C_4H_6O_2$ in the isoprene + NO_3 system, and a few CHO compounds in the α -pinene and β -caryophyllene systems. These compounds are likely related to artefacts from the electrospray ionization (Goracci et al., 2017; James et al., 2006; Keith-Roach, 2010; Maire and Lange, 2010; Kourtchev et al., 2020; Rovelli et al., 2020). They may ~~occurring~~ due to the proximity of $-ONO_2$ functional groups next to peroxy linkages which results in fragmentation when exposed to water in the electrospray 330 (Bell et al, in preparation), and a loss of a HNO_3 fragment during ionization (Liu et al., 2019).

3.3 Photolytic aging of isoprene, α -pinene and β -caryophyllene BSOA_{NO3}

As can be observed in Fig. 1, switching on the lights has effects on particle mass and size for all BSOA_{NO3} systems, but with different extent. For the isoprene SOA, the particle size and mass show a slightly steeper decrease compared to the situation expected without UV irradiation (dashed lines). For the α -pinene SOA, both the particle size and mass decrease compared to the dark, from 229 nm and a normalized mass concentration of 0.9 to 219 nm and 0.87 after 1 h photolysis. The β -caryophyllene SOA, although the least volatile, shows a decrease by 12 % (normalized mass concentration of 0.83 versus 0.95 expected without UV irradiation), and a shrinking of the mean particle size from 273 nm to 230 nm. These results indicate that there are slight to moderate losses of particle phase compounds due to UV irradiation. The possible reasons causing the differences in the three systems will be discussed in this section and in section 3.5.

In Fig. 3, the relative changes in the chemical composition of the SOA before (pre) and after (post) photolytic aging measured by the FIGAERO-CIMS are illustrated. During irradiation, processes/reactions occurring in the dark may also continue with the lights on, e.g. consumption/decomposition of reactive oxygen species (Pospisilova et al., 2020), evaporation of semi-volatile compounds, and hydrolysis of nitrate functional groups can alter the chemical composition of SOA particles. To account for this, Fig. 3 compares the chemical composition of two particle filter samples collected during dark aging (Pre 1 and Pre 2), and one filter sample after 1 h of photolytic aging (Post). The time interval of the sampling was about 1.5–2 h or about 3 h if a particle blank was performed between two filters. The difference between the two filters during dark aging (Pre 2 – Pre 1) shows the changes of the chemical composition caused by all other processes than photolysis, while the difference between the last filter during dark aging and the one after 1 h photolysis (Post – Pre 2) shows the impacts of the above-mentioned processes plus the impact caused by UV irradiation.



350

Fig. 3 Relative changes of the fraction of the total signal between two filters during dark aging (Pre 2 – Pre 1) and between the last filter during dark aging and one filter after 1 h of photolysis (Post – Pre 2), for (a) Exp. 1: isoprene + NO₃, (b) Exp. 3: α -pinene + NO₃, and (c) Exp. 4: β -caryophyllene + NO₃.

The comparison between the two filters during dark aging (Pre 2 – Pre 1 in Fig. 3) shows relatively small changes of the chemical composition that are similar for all three systems: the mass fractions of high molecular weight compounds increase and the mass fractions of low molecular weight compounds decrease. The signal fraction changes of individual compounds are less than 2 %. Such change is mainly due to evaporation of semi-volatile compounds, as gas-phase wall losses act as a sink for semi-volatile compounds, resulting in the repartitioning of the particle phase (Bertrand et al., 2018). Bell et al. (2021) Bell et al. (2021) show in the α -pinene SOA system that most of the changes in chemical composition occur over the first 2 h of dark aging, meaning at the time directly prior to photolysis the chemical composition has mostly stabilized. [Fig S7 in the SI shows the changes in absolute signal fraction for the filter samples pre and post photolysis for Exp. 3.](#)

During photolysis, the changes observed in the mass spectral patterns (Post – Pre 2 in Fig. 3) differ from those during dark aging, and have a larger magnitude. For the isoprene system, the compounds exhibiting the largest decays in signal fraction are $C_{10}H_{17}N_3O_{12-13}$ and $C_{10}H_{16}N_4O_{14-15}$ (8 % and 2 % of the total signal, respectively). At the same time, there are a few compounds, e.g. $C_9H_{14}N_2O_7$ and $C_{10}H_{14}N_2O_9$, whose signal fractions increase (< 1 %). For the α -pinene system, the main dimer compounds ($C_{20}H_{32}N_2O_{8,9,10}$) decrease by 13.6 % of the total signal during photolysis, while a few monomers, e.g. $C_9H_{15}NO_{6,8}$, $C_{10}H_{15}NO_{8-9}$ increase by up to 2 %. The β -caryophyllene SOA system shows decreases of signal fractions of both monomers and dimers, mainly $C_{15}H_{25}NO_8$, $C_{15}H_{23}NO_9$ and $C_{15}H_{26}N_2O_9$, and $C_{30}H_{48}N_2O_{11-13}$, while the mass fractions of quite a few compounds including C_{12-14} compounds (e.g. $C_{14}H_{23}NO_{6,7}$), C_{15} compounds (e.g. $C_{15}H_{23}NO_6$, $C_{15}H_{25}N_2O_8$), C_{16-29} compounds (e.g. $C_{29}H_{46}N_2O_{9-11}$) and C_{30} compounds (e.g. $C_{30}H_{46}N_2O_{12}$) increase. Overall, our results show that the major compounds decomposing during photolysis are both monomers and oligomers and that there are also compounds formed that contain fewer carbon numbers and/or fewer nitrate groups.

The FIGAERO-CIMS offers insight into the pre- vs. post-photolysis SOA composition, and the EESI-TOF allows monitoring the evolution of individual compounds at high time resolution. Using a linear fit to the 2 h pre-photolysis time series of the individual compounds measured by the EESI-TOF and comparing a predicted value based on this fit at 1h post photolysis (with 95 % confidence interval) with the actually measured signal (see the SI, Fig. [S6S8](#)), we find that 54 (the average value from Exp. 1 and Exp. 2) out of 359, 24 out of 158 and 104 out of 441 compounds decreased significantly during photolysis, i.e., by $44\% \pm 20\%$, $64\% \pm 24\%$, and $24\% \pm 18\%$, for the isoprene, α -pinene and β -caryophyllene SOA, respectively. These compounds contributed [4853 %](#), [445 %](#) and [602 %](#) to the total pre-photolysis [signal-mass](#) for these three systems. Meanwhile, there were 116, 53, and 164 compounds that increased during photolysis for the isoprene, α -pinene and β -caryophyllene SOA, respectively. We note, however, that the fraction appearing to be resistant to photolysis or even showing increase may undergo functional group changes during photodegradation even if the molecular formula appears unchanged during exposure to UV light, or that decay of molecules with a specific molecular formula may be compensated by production of molecules with this formula through the decay of other molecules. Here, we cannot fully exclude the particle-phase compounds volatilization resulting from an increase in chamber temperature (3–4 °C, caused by heating from the chamber lights). However, because most of the compounds showing decays are oligomers with very low predicted volatilities, such an increase in temperature is unlikely to play a major role in the change in/of composition.

Figure 4 shows the time series of the main compounds that degraded during photolysis for each system, measured by both the EESI-TOF and the FIGAERO-CIMS. Within the error tolerances, the time series of the compounds measured by the two instruments have a good agreement. The decay rates of these compounds are compound-dependent. Even though 1 h of photolytic aging might be too short to observe full decay trajectories (Zawadowicz et al., 2020; O'Brien and Kroll, 2019), it is long enough to distinguish the non-photolabile compounds and the photolabile compounds, and compare the decay rates of the photolabile compounds (Henry and Donahue, 2012; Wong et al., 2015). As also shown by Nah et al. (2016), most of the changes of α -pinene + NO_3 SOA due to photochemical aging happened in the first 1 h of light exposure.

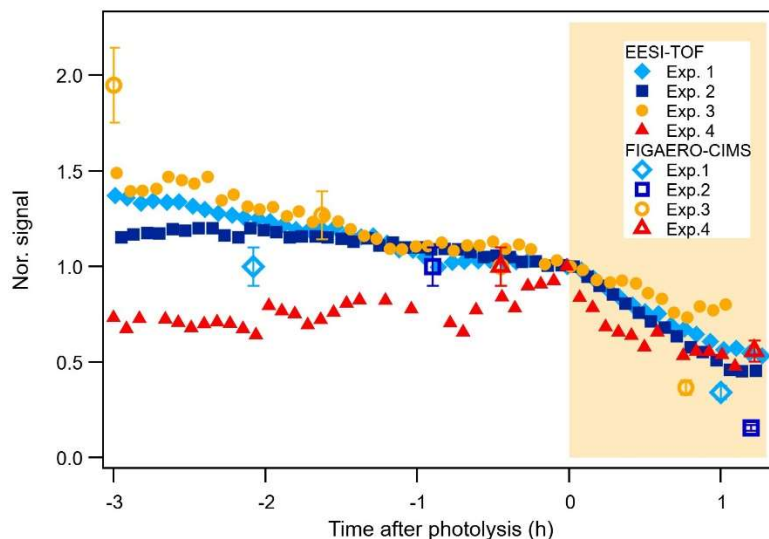


Fig. 4 Time series of the isoprene tracers $\text{C}_{10}\text{H}_{17}\text{N}_3\text{O}_{12,13}$ (Exp.1 and Exp. 2), the α -pinene tracers $\text{C}_{20}\text{H}_{32}\text{N}_2\text{O}_{8-10}$ (Exp. 3) and the β -caryophyllene tracers $\text{C}_{30}\text{H}_{48}\text{N}_2\text{O}_{8-10}$ (Exp. 4) from the EESI-TOF and the FIGAERO-CIMS.

Photolysis requires chromophores, which absorb particular wavelengths of visible light. Earlier studies of photodegradation of OH- and O_3 -initiated SOA under low- NO_x conditions have demonstrated that photolysis fragments molecules with functional groups like carbonyls ($\text{C}=\text{O}$) and peroxides ($\text{R}-\text{O}-\text{O}-\text{R}$) (Surratt et al., 2006; Walser et al., 2007; Mang et al., 2008; Pan et al., 2009; Krapf et al., 2016). In contrast to these studies, the $\text{BSOA}_{\text{NO}_3}$ in our study is rich in nitrate groups and oligomers. In Fig. 5a, we plot the average number of nitrate groups per monomer (monomer unit) for the three FIGAERO-CIMS filter samples (the same as in Fig. 3) selected before and after photolysis for all three SOA systems. Overall, the particle-phase compounds of all three SOA types contain on average a similar number of nitrate groups per monomer (1–1.5). During the last 2–3 h of dark aging, the nitrate group fraction is stable, but photolysis causes a slight decrease of the nitrate-to-monomer ratio for all systems, consistent with the decrease of 1–3 % of the mass fraction of ONs of total organic compounds for all systems. It is clear from this that UV light fragmentation of nitrate groups only plays a minor role in changing the chemical composition of SOA when transitioning from dark to light conditions. It is known that organic nitrates can undergo photolysis and release NO_2 via $\text{RONO}_2 + h\nu \rightarrow \text{RO}\cdot + \text{NO}_2$ (Barnes et al., 1993). Measurements of the absorption cross-sections of a number of alkyl

415 nitrates, such as methyl nitrate, and some bifunctional organic nitrates have shown lifetimes up to between 14 h and 6 days (Barnes et al., 1993). The absorption cross-sections of organic nitrates normally have an absorption maximum at $\lambda < 290$ nm and start to decrease when $\lambda > 310$ nm (Barnes et al., 1993; He et al., 2021). The blacklights in the chamber reproduce the solar spectrum well in the range of 320–400 nm but the intensity at lower wavelengths (< 320 nm) falls off faster than the solar spectrum. Thus, the photolysis of nitrate groups observed in our study represents a lower limit of that would be expected in the atmosphere. More recent studies have shown that the presence of a nitrate group can enhance the absorption cross sections and make the photolysis of carbonyl nitrates faster than their reaction with OH (Müller et al., 2014; Suarez-Bertoa et al., 2012).
 420 However, based on the stability of the nitrate group fraction during photolytic aging as described above (compare also Fig. 5), the cleavage of the nitrate functional group from the carbon chain is not the main loss pathway in our study and on the time scales of our experiments.

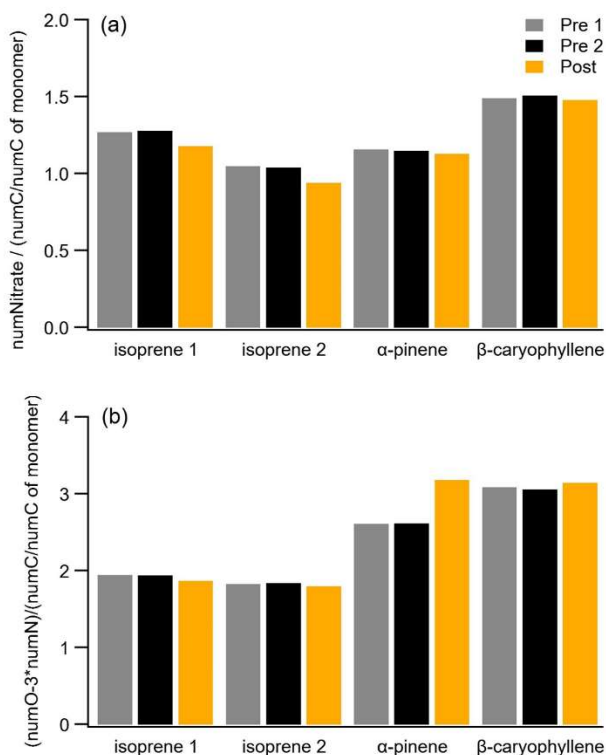


Fig. 5 Mass-weighted number of nitrate groups to monomer (number of carbon/number of the carbon atoms in precursors (5, 10 and 15 for the isoprene, α -pinene and β -caryophyllene SOA, respectively)) ratio and mass-weighted number of non-nitrate oxygen to monomer ratio for three filters (Pre 1, Pre 2 and Post) for all experiments.

425 In terms of oligomers, for the α -pinene and β -caryophyllene systems, the major degrading compounds are C_{20} and C_{30} dimers, while the major compounds formed are their corresponding C_{10} and C_{15} monomers (the isoprene system is a mix of C_{10} dimers, C_{15} trimers and C_{20} tetramers, which makes it challenging to identify the potential parent compounds for those newly formed

compounds). This indicates that for some fraction of the oligomers, the linkage between two monomer blocks is photolabile. Oligomers may be formed through both gas- and particle-phase processes. As $RO_2 + R'O_2 \rightarrow ROOR' + O_2$ is the main reaction channel for RO_2 self- and cross-reactions in the gas phase, a large fraction of peroxides can be expected, and such mechanisms of dimer formation of the isoprene + NO_3 SOA were proposed (Ng et al., 2008; Zhao et al., 2020; Wu et al., 2020). Recent studies also showed multiple pathways of dimerization in the particle phase or the gas-particle interface (Zhao et al., 2019; Claflin and Ziemann, 2018). All the studies mentioned above show that formation of dimers, in both the gas- and particle-phases, changes the functional groups of the resulting molecules compared to their building blocks (monomers). It is likely that peroxide functional groups are formed during RO_2 self- / cross-reactions, which could make some dimers photolabile, while the formation of potentially photolabile carbonyl functional groups is less certain from NO_3 oxidation.

Some of the compounds being formed during photolytic aging are molecules with 1-3 fewer carbon atoms than their potential parent compounds (e.g. C_{13} , C_{14} , C_{29} compounds in the β -caryophyllene system), indicating fragmentation of the carbon skeleton. On average, each monomer (or monomer unit) of the isoprene, α -pinene and β -caryophyllene SOA contains ca. 2, 2.5, and 3 oxygen atoms pre photolysis (disregarding the oxygen atoms in the nitrate groups), respectively (Fig. 5b), suggesting that in addition to nitrate groups, these compounds also possess other oxygenated functional groups, and other possible chromophores. The β -caryophyllene SOA exhibited higher losses of the particle mass and reduction in size (Fig. 1), followed by the α -pinene SOA, which could partly be explained by its higher number of functional groups per monomer (or monomer unit), i.e. larger photolabile fraction, compared to the other two systems.

Overall, the particle mass loss of nitrate-initiated SOA after 1h photolysis in our study is less than that reported for the OH- and O_3 -initiated SOA under low- NO_x conditions (Zawadowicz et al., 2020; Wong et al., 2015; Henry and Donahue, 2012; Epstein et al., 2014), despite observing larger changes in the chemical composition. One possible reason could be that our systems have a large fraction of oligomers and photolysis-derived products may not directly evaporate, meaning a substantial fraction of these products retain low enough volatility to remain in the particle phase. In addition, in terms of different functional groups, addition of a nitrate group in a given molecule is estimated to reduce its vapour pressure by about 2.5 orders of magnitude, which is comparable to other oxygenated functional groups often observed in the OH- and O_3 -initiated BSOA, e.g. the hydroxyl group ($-OH$) and hydroperoxy group ($-OOH$) (2.4–2.5 orders of magnitude), or the carbonyl group ($=O$) (1 order of magnitude) (Pankow and Asher, 2008; Donahue et al., 2011). Thus, the gas-phase compounds formed in our systems could contain less functional groups (disregarding nitrate groups) than those in OH- and O_3 -initiated BSOA, but still be of low enough volatility to condense into the particle phase. The elemental oxygen-to-carbon (O:C) ratio (disregarding the oxygen atoms in the nitrate groups) of the α -pinene SOA was calculated to be 0.26 ± 0.01 before photolysis in Exp. 3, which is lower than the reported O:C ratios of 0.34–0.36 for BSOA from ozonolysis of α -pinene measured by the FIGAERO-CIMS in laboratory experiments (Huang et al., 2018). As shown above, nitrate groups might be less photolabile than carbonyls and peroxides, thus different sensitivities towards photolysis can be expected for the systems initiated by different oxidants.

460

3.4 Changes in the gas phase during photolysis

The primary focus of this study is on the changes in condensed-phase chemical composition of BSOA_{NO3} due to photolytic aging. However, we cannot decouple processes happening in both particle and gas phases. For example, photo-degradation of semi-volatile compounds in the gas phase could lead to a decrease of compounds in the particle phase as they will evaporate to re-establish equilibrium. If gas-phase photo-degradation was the dominant cause for mass loss in all systems, then the largest decays in the particle phase would be expected from the most volatile species. Further, large non-volatile molecules (e.g. dimers in the β -caryophyllene SOA) should be non-responsive to such a pathway. Because there is a systematic degradation of dimers in all systems, it is unlikely that repartitioning derived from gas-phase photodegradation is driving the change in SOA composition during UV aging.

465
470 For the experiments shown here, the FIGAERO-CIMS using I⁻ as the reagent ion (and an x-ray generator as the ion source) also measured the gas phase. However, in systems with a high abundance of NO₃ radicals, charge transfer can cause losses of I⁻ and formation of NO₃⁻ (Lee et al., 2014). Additionally, the reaction of N₂O₅ and I⁻ may partly result in NO₃⁻ + INO₂, and H transfer reactions can occur between I⁻ and HNO₃ (HNO₃ can come from the hydrolysis of N₂O₅ in our injection inlet or on chamber walls), both providing other routes to the formation of NO₃⁻. As the amount of NO₃⁻ introduced in our systems was
475 very high, the signal of NO₃⁻ was comparable to and sometimes even higher than the signal of I⁻. Thus, gas-phase compounds were detected clustered with both NO₃⁻ and I⁻, with changing ratios of I⁻/NO₃⁻ during the experiments (higher during dark aging and lower during photolysis). This was not an issue for the particle phase, as particles are desorbed from the filter with pure nitrogen. We probed the uncertainties of detected signals due to the changing I⁻/NO₃⁻ ratio (from ~0.1 to 1.6) after Exp. 2 (details see the description in the SI and Fig. S43). In our system, for those compounds clustered with I⁻, the normalized signal
480 didn't change significantly with decreasing I⁻/NO₃⁻ as long as I⁻/NO₃⁻ was higher than ~0.3, but it decreased by about 20–40 % when I⁻/NO₃⁻ decreased further to 0.1, as more molecules were clustered with NO₃⁻.

Taking these uncertainties into account, we found that for the β -caryophyllene SOA, the signal of the major gas-phase compounds either stayed stable (e.g. C₁₅H₂₅NO_{5,6,7}) or increased significantly (e.g. C₁₄H₂₃NO₄, C₁₅H₂₃NO₆, C₁₅H₂₆N₂O₈, with increases of the normalized signals of more than 5 times) during photolytic aging. For the isoprene and α -pinene SOA, although
485 the low I⁻/NO₃⁻ ratio (< 0.1) hindered a quantitative comparison, we still observed increases of several major compounds (e.g. C₅H₁₀N₂O₈ for the isoprene SOA, C₁₀H₁₅NO₈, C₁₀H₁₇NO₇ for the α -pinene SOA). These are likely fragmentation products from oligomers and/or monomers. As the volatility of these small compounds is much higher than their parent oligomer compounds, they would tend to entirely or partly (depending on their volatility) evaporate to the gas phase. Different from the photolytic aging of O₃- or OH- initiated SOA, we did not however observe a significant increase of the signals of small acids
490 in the gas phase, such as formic acid and acetic acid (Pan et al., 2009), despite observations of fragmentation reactions in the particle phase. Their minor importance seems not to significantly impact the measured formic or acetic acid in the gas phase. In addition to photolytic aging of gas-phase compounds, there are other gas-phase reactions initiated by UV irradiation, which may impact the chemical composition, e.g. OH oxidation, and the reactions with O₃ or NO₃ radicals. In our experimental

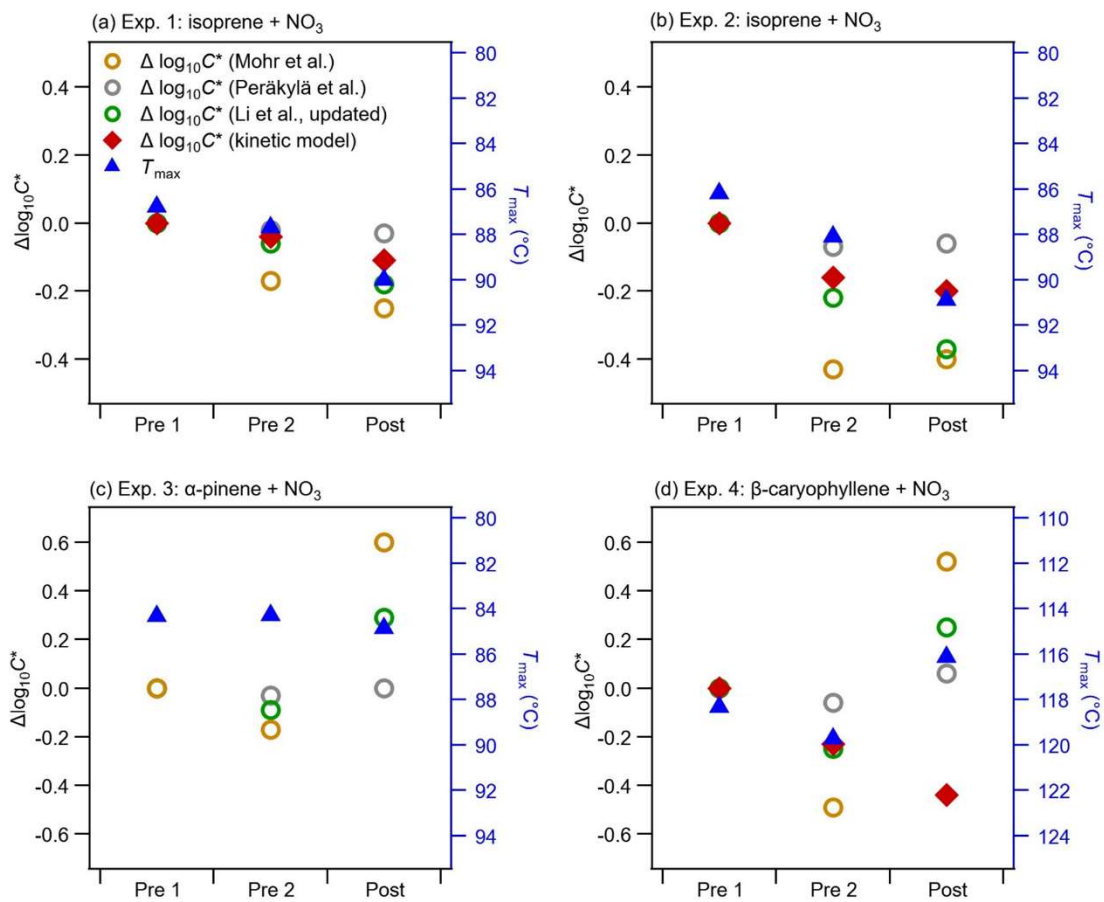
495 conditions (200+ ppb NO₂ from decomposition of N₂O₅), if there are any OH radicals formed, then they will nearly exclusively
react with NO₂ given the high concentrations. However, we didn't observe significant increase in the gas-phase HNO₃ signal.
For the reactions with O₃ or NO₃, if there were appreciable such reactions in the experiments with isoprene and β-
caryophyllene, where double bonds are still present, we would expect to observe significant formation of more highly
oxygenated molecules, which are absent in Fig. 3. Additionally, Fig. 3 shows there is a consistent degradation of dimers in all
systems, including α-pinene where double bonds are not retained, thus suggesting the dominant photolytic degradation
500 pathways are independent of gas-phase chemistry.

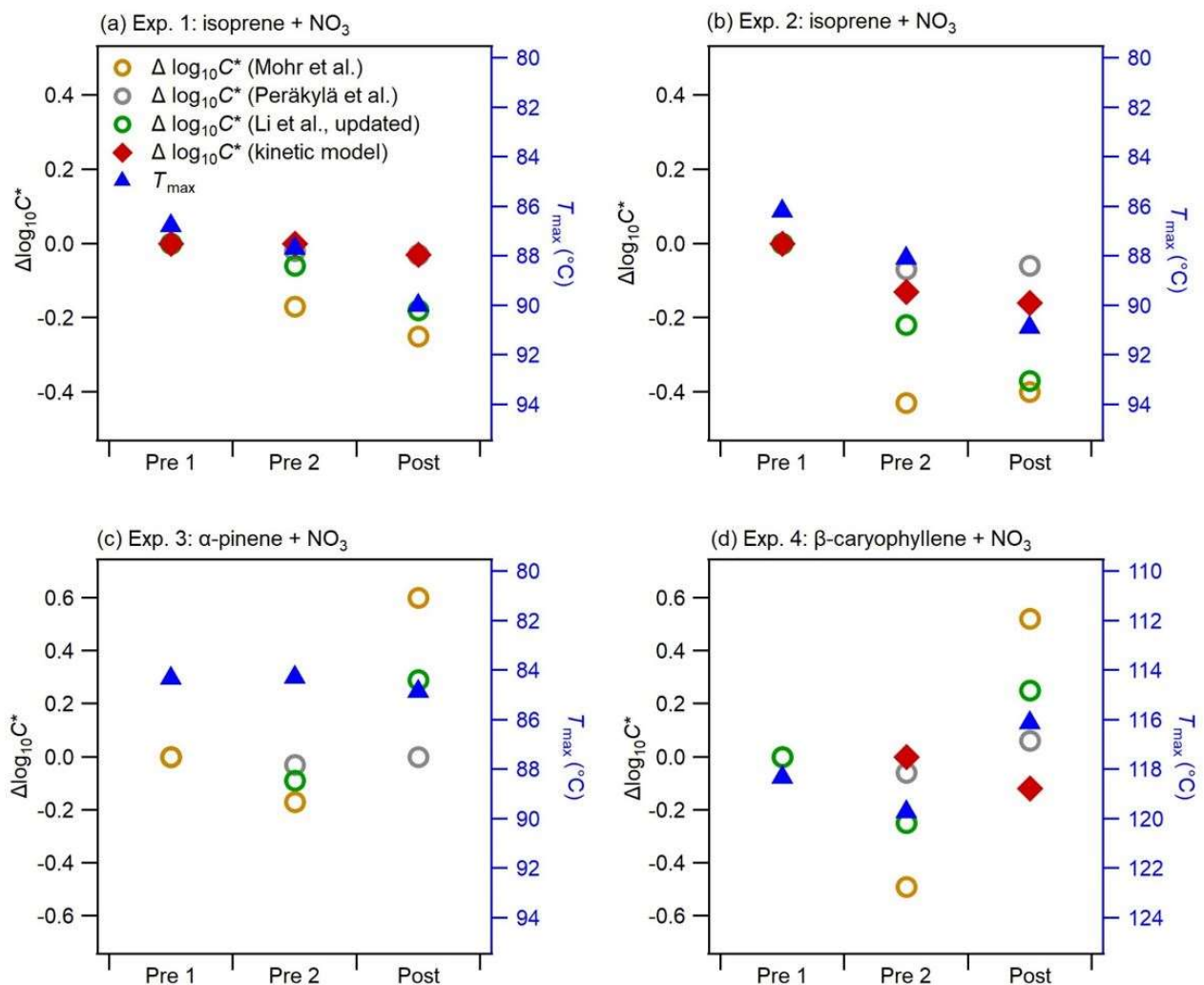
3.5 Impacts of photolysis on particle volatility

Considering photolytic aging results in the degradation of molecules, there is a shift of the volatility distribution towards higher
volatility species, which can cause evaporation of particulate mass. Here we discuss how the apparent volatility of remaining
particles changes during photolytic aging, and the potential influence the chemical processes discussed previously have on
505 these changes.

Figure 6 shows the changes in the bulk volatility derived from different methods (bulk log₁₀C* derived from molecular
composition using different parametrizations, bulk log₁₀C* derived from the kinetic model using the VTDMA measurements,
and mass-weighted average T_{max} from the FIGAERO-CIMS thermograms) during dark aging and photolysis for all BSOA_{NO3}
systems. Note that we show the Δlog₁₀C* (calculated by subtracting the bulk log₁₀C* of the filter Pre 1 from the bulk log₁₀C*
510 of each filter), since the variabilities in the absolute bulk log₁₀C* calculated by different parameterizations span several orders
of magnitude: the bulk log₁₀C* for all three systems is in the range of -11.9–7.6 based on the parameterization by Mohr et al.
(2019), -3.7–0.3 by Li et al. (2016) and Isaacman-VanWertz and Aumont (2021), and -0.5–0 by Peräkylä et al. (2020) (see
the SI, Fig. S97). As Fig. S10 in the SI shows, the discrepancy of log₁₀C* from the three parameterizations becomes larger with
increasing nitrogen number. Whereas a detailed discussion on these discrepancies is beyond the scope of this paper, they
515 clearly reflect the uncertainties related to volatility estimates of complex organic particles (O'Meara et al., 2014; Wu et al.,
2021). T_{max} is a qualitative measure of volatility, and is influenced by filter mass loadings, temperature ramp rate, and
FIGAERO geometry (Huang et al., 2018; Schobesberger et al., 2018; Thornton et al., 2020). However, T_{max} variation due to
these factors is generally smaller than the difference in monomers and dimers. We compared the shape of thermograms and
T_{max} of several monomers and dimers observed in our study to that of the same compounds from a few field campaigns (see
520 the SI, fig. S118). Overall, the thermal desorption behaviour observed in our chamber experiments is similar compared to this
from field measurements. By further comparing the log₁₀C* of individual compounds based on e.g. Mohr et al. (2019) with
their corresponding T_{max} (Fig. S129), we found good qualitative agreement with a clear trend of increasing T_{max} with decreasing
log₁₀C*, and higher T_{max} for dimers than corresponding monomers for all systems. a generally good qualitative agreement, but
We also noticed large uncertainties in the calculated log₁₀C*, especially for ON oligomers with multiple nitrate groups. For
525 example, the dominating dimer C₂₀H₃₂N₂O₉ has a T_{max} of about 70 °C, which is in the range of T_{max} of C₁₀ monomers such as

$C_{10}H_{15}NO_9$. However, based on the parameterization of Mohr et al. (2019), the $\log_{10}C^*$ of the dimer $C_{20}H_{32}N_2O_9$ (-7.9) is much lower than the $\log_{10}C^*$ of the C_{10} monomers ($\log_{10}C^* > -5$).





530 **Fig. 6** Comparison of changes in the bulk volatility measured with three methods before and after photolysis (Pre 1, Pre 2 and Post) for all experiments. Method 1: $\Delta \log_{10} C^*$ based on the parameterizations of Mohr et al. (2019), Li et al. (2016) (updated by Isaacman-VanWertz and Aumont (2021)), and Peräkylä et al. (2020); Method 2: mass-weighted average T_{\max} (note the right axes are swapped, and the range in (d) is different from that in others); Method 3: $\Delta \log_{10} C^*$ from the kinetic model (data available only for Pre 2 and Post in Exp. 4).

535 Overall, for the two isoprene experiments (Exp. 1 and Exp. 2), almost all methods show a decrease in volatility as the experiment progresses, with no change in trend during the transition from dark to light conditions. This agrees well with the changes in the chemical composition as shown in Fig. 3: during dark aging, the chemical composition shifts to higher mass (lower volatile) compounds and causes a decrease in the bulk volatility; during photolysis, there is additional decay of some oligomers such as $C_{10}H_{17}N_3O_{13}$, whose volatility is in the intermediate range of all compounds (Fig. S129). As a consequence,

540 despite clear changes in the chemical composition, the bulk volatility does not change substantially due to photolysis. In Exp.

2, the $\Delta\log_{10}C^*$ by both Peräkylä et al. (2020) and Mohr et al. (2019) decreased during the dark aging but increased slightly during photolysis, which is different compared to other methods. The difference between Exp. 1 and Exp. 2 is probably due to the differences in the chemical composition (Fig. 2 vs. Fig. S65) as Exp. 1 had higher NO_3 /isoprene ratio and the SOA with more nitrate groups (Fig. 5), and also due to different mechanisms to treat nitrate groups in the different parameterizations. It reflects again uncertainties related to volatility estimates by different parameterizations.

In Exp. 3 (α -pinene + NO_3), no clear trend in volatility can be discerned. T_{\max} does not exhibit significant changes during both dark aging and photolysis. However, the $\Delta\log_{10}C^*$ by the parameterizations shows a slight decrease during the dark aging and an increase during photolysis. As shown in Fig. 3, we observed decreases of a few dimers and increases of a few monomers, which, based on the parameterizations, causes a shift from low volatile compounds to high volatile compounds. However, as mentioned above, the T_{\max} of these dimers is not necessarily higher than those monomers, i.e., the volatility of these dimers is not necessarily lower than that of those monomers. Thus, the mass-weighted average T_{\max} doesn't decrease. Unfortunately, no VTDMA data are available for this experiment.

In Exp. 4 (β -caryophyllene + NO_3), the different methods yield different information on the relative changes of volatility from dark to photolytic aging. Both T_{\max} and $\Delta\log_{10}C^*$ from the parameterizations show the bulk volatility decrease during dark aging and increase during photolysis, which would agree with changes in chemical composition. The shift from small (high volatile) compounds to large (low volatile) compounds during dark aging causes the decrease in the bulk volatility, while during photolysis the major compounds that decay cover both monomers and oligomers with a wide range of volatility, and there are a few newly formed $C_{<15}$ compounds that remain in the particle phase (Fig. 3), thus the bulk volatility increases.

However, the $\Delta\log_{10}C^*$ from the VTDMA data doesn't agrees with the trend ~~during dark aging but not~~ during photolysis. We note that in Exp. 1–3, the particle size distribution and mean particle size, as shown in Fig. 1, did not change substantially, while in Exp. 4 (β -caryophyllene + NO_3), the particles size became significantly smaller during photolysis (Fig. 1). In Fig. 7, the evolution of the volume distribution of the β -caryophyllene SOA in Exp. 4 shows the size distribution slowly shifts to larger sizes during dark aging, but during photolysis the decrease in particles with diameters larger than 300 nm is much greater than the decrease in small particles, indicating that the photo-degradation is dependent upon particle size. The size dependence can be explained by calculating the mass absorption efficiency as a function of particle size (see the SI, Fig. S5S4), which shows particles with a diameter of 300 nm are 1.5–1.7 times more efficient in absorbing the chamber lights ($\lambda = 350$ nm) than 100 nm particles. Other processes, such as coagulation and evaporation, tend to lead to larger decreases of smaller particles, which is opposite to what we found here, while the wall loss rate (which is tested in another experiment during the same campaign) was nearly constant for the particle size range up to 400 nm, thus unlikely the reason for size dependence of light absorption. In comparison, the isoprene and α -pinene systems have smaller and narrower size distribution, and consequently do not have an equally important size-dependence in their response to UV light. This could also partly explain why the β -caryophyllene SOA had the largest decay in particle mass and size among the three systems. As the particles with different sizes will not have a uniform change in their chemical composition, the volatility measured for one selected size by the VTDMA may not be able to represent the change in the bulk volatility for experiments with a wide distribution of particle

575 sizes—similarly, caution should be applied when interpreting the representativeness of measurements based on the bulk mass for the whole particle size distribution.

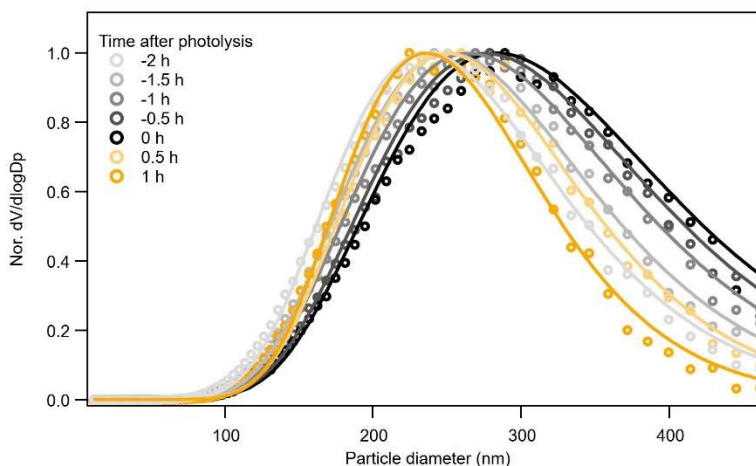


Fig. 7 Evolution of particle size distribution of the β -caryophyllene SOA during dark aging and photolysis. The solid lines are lognormal fittings.

580 4. Conclusion & Atmospheric Implications

Our experimental observations on three BSOA_{NO₃} systems show that the dark-to-light transition (1 h photolytic aging) causes slight to moderate evaporation in BSOA_{NO₃} (~0, 3.5 and 12 % of the total mass for the isoprene, α -pinene and β -caryophyllene SOA, respectively). Evaporation is due to the fragmentation of photolabile compounds and formation of volatile fragmentation products. Despite finding 0–12 % of the mass evaporating during photolysis, 48.53 %, 44.5 % and 60.2 % of the total **signal mass** of the isoprene, α -pinene, and β -caryophyllene SOA, respectively, is sensitive to photolytic aging, representing a majority of the pre-photolysis composition.

Fragmentation of nitrate groups is not the main loss pathway on the time scale of our experiments. For all BSOA_{NO₃} studied here, UV light fragments oligomers at the linkage between the monomer units (likely peroxides), as well as functional groups at other positions, causing the formation of monomers and compounds with shorter carbon skeleton (e.g. C₁₀ \rightarrow C₉). The newly formed compounds are more volatile than their parent compounds, and are thus entirely/partly released back into the gas phase. The changes in bulk volatility vary with individual experiments, and depend on (1) whether the volatility of photolabile fractions is higher/lower than that of non-photolabile fractions (2) how the fragment products remain in the particle phase. The comparisons of different methods to assess the bulk volatility reveal the complexity of volatility assessments. There is generally a good agreement with the trends between the VTDMA and thermal desorption behaviour from the FIGAERO-CIMS (both desorption-based methods). However, the uncertainties related to molecular formula-derived parameterization, especially for the compounds with multiple nitrate groups, likely causes disagreement when assessing the changes in the absolute bulk

volatility. It is also worth noting that particle size dependence of light absorption should be considered when studying the changes in the bulk volatility for systems with broad size distributions.

Our systems represent conditions in which $\text{RO}_2\text{-RO}_2$ and $\text{RO}_2\text{-NO}_3$ reactions are favoured and ON oligomers contribute to the high SOA yields we observed. Different changes in particle mass/size due to photolysis could be expected for the $\text{BSOA}_{\text{NO}_3}$ formed under different conditions, as they have different chemical composition, thus different amounts and/or types of chromophores. In addition, the differences among the three BVOC systems also indicate that results obtained for specific BVOC cannot directly be generalized to SOA present in the atmosphere and it is necessary to study different BVOC-SOA systems.

To our knowledge, the photolysis of SOA has so far been studied mainly under low- NO_x conditions. The sensitivity of ONs to UV light is poorly understood. As ONs are important in high- NO_x environments and make substantial contributions to the total organic aerosols (Farmer et al., 2010; Lee et al., 2016), future studies that probe the photolytic aging of ONs under different ambient conditions and for different SOA precursors are needed to improve our understanding of the life cycle of ONs.

610 **Data availability**

The datasets are available upon request to the corresponding authors.

Author contributions

CW, DMB and CM designed the study. Chamber experiments were carried out by CW, DMB, ELG, SH, AB, SG and CM. Data analysis and interpretation was performed by CW, DMB, ELG, IR, JS and CM. CW wrote the manuscript, with input from all co-authors. All co-authors read and commented on the manuscript.

Competing interests

The authors declare that they have no conflict of interest.

Acknowledgements

This work was supported by the EUROCHAMP-2020, ~~and~~ the Knut and Alice Wallenberg Foundation (WAF project CLOUDFORM, grant no. 2017.0165), and H2020 European Research Council (CHAPAs, grant no. 850614).

References

- 625 Bannan, T. J., Le Breton, M., Priestley, M., Worrall, S. D., Bacak, A., Marsden, N. A., Mehra, A., Hammes, J., Hallquist, M., Alfarra, M. R., Krieger, U. K., Reid, J. P., Jayne, J., Robinson, W., McFiggans, G., Coe, H., Percival, C. J., and Topping, D.: A method for extracting calibrated volatility information from the FIGAERO-HR-ToF-CIMS and its experimental application, *Atmos. Meas. Tech.*, 12, 1429-1439, 10.5194/amt-12-1429-2019, 2019.
- 630 Barnes, I., Becker, K. H., and Zhu, T.: Near UV absorption spectra and photolysis products of difunctional organic nitrates: Possible importance as NO_x reservoirs, *Journal of Atmospheric Chemistry*, 17, 353-373, 10.1007/BF00696854, 1993.
- Bell, D. M., Wu, C., Bertrand, A., Graham, E., Schoonbaert, J., Giannoukos, S., Baltensperger, U., Prevot, A. S. H., Riipinen, I., El Haddad, I., and Mohr, C.: Particle-phase processing of α -pinene NO₃ secondary organic aerosol in the dark, *Atmos. Chem. Phys. Discuss.*, 2021, 1-28, 10.5194/acp-2021-379, 2021.
- 635 Bertrand, A., Stefenelli, G., Jen, C. N., Pieber, S. M., Bruns, E. A., Ni, H., Temime-Roussel, B., Slowik, J. G., Goldstein, A. H., El Haddad, I., Baltensperger, U., Prévôt, A. S. H., Wortham, H., and Marchand, N.: Evolution of the chemical fingerprint of biomass burning organic aerosol during aging, *Atmos. Chem. Phys.*, 18, 7607-7624, 10.5194/acp-18-7607-2018, 2018.
- Clafin, M. S., and Ziemann, P. J.: Identification and Quantitation of Aerosol Products of the Reaction of β -Pinene with NO₃ Radicals and Implications for Gas- and Particle-Phase Reaction Mechanisms, *The Journal of Physical Chemistry A*, 122, 3640-3652, 10.1021/acs.jpca.8b00692, 2018.
- 640 Daellenbach, K. R., Uzu, G., Jiang, J., Cassagnes, L.-E., Leni, Z., Vlachou, A., Stefenelli, G., Canonaco, F., Weber, S., Segers, A., Kuenen, J. J. P., Schaap, M., Favez, O., Albinet, A., Aksoyoglu, S., Dommen, J., Baltensperger, U., Geiser, M., El Haddad, I., Jaffrezo, J.-L., and Prévôt, A. S. H.: Sources of particulate-matter air pollution and its oxidative potential in Europe, *Nature*, 587, 414-419, 10.1038/s41586-020-2902-8, 2020.
- Daumit, K. E., Kessler, S. H., and Kroll, J. H.: Average chemical properties and potential formation pathways of highly oxidized organic aerosol, *Faraday Discussions*, 165, 181-202, 10.1039/C3FD00045A, 2013.
- 645 Donahue, N. M., Epstein, S. A., Pandis, S. N., and Robinson, A. L.: A two-dimensional volatility basis set: 1. organic-aerosol mixing thermodynamics, *Atmos. Chem. Phys.*, 11, 3303-3318, 10.5194/acp-11-3303-2011, 2011.
- Epstein, S. A., Riipinen, I., and Donahue, N. M.: A Semiempirical Correlation between Enthalpy of Vaporization and Saturation Concentration for Organic Aerosol, *Environmental Science & Technology*, 44, 743-748, 10.1021/es902497z, 2010.
- 650 Epstein, S. A., Blair, S. L., and Nizkorodov, S. A.: Direct Photolysis of α -Pinene Ozonolysis Secondary Organic Aerosol: Effect on Particle Mass and Peroxide Content, *Environmental Science & Technology*, 48, 11251-11258, 10.1021/es502350u, 2014.
- Farmer, D. K., Matsunaga, A., Docherty, K. S., Surratt, J. D., Seinfeld, J. H., Ziemann, P. J., and Jimenez, J. L.: Response of an aerosol mass spectrometer to organonitrates and organosulfates and implications for atmospheric chemistry, *Proceedings of the National Academy of Sciences*, 107, 6670-6675, 10.1073/pnas.0912340107, 2010.
- 655 Faxon, C., Hammes, J., Le Breton, M., Pathak, R. K., and Hallquist, M.: Characterization of organic nitrate constituents of secondary organic aerosol (SOA) from nitrate-radical-initiated oxidation of limonene using high-resolution chemical ionization mass spectrometry, *Atmos. Chem. Phys.*, 18, 5467-5481, 10.5194/acp-18-5467-2018, 2018.
- Fry, J. L., Draper, D. C., Barsanti, K. C., Smith, J. N., Ortega, J., Winkler, P. M., Lawler, M. J., Brown, S. S., Edwards, P. M., Cohen, R. C., and Lee, L.: Secondary organic aerosol formation and organic nitrate yield from NO₃ oxidation of biogenic hydrocarbons, *Environmental science & technology*, 48, 11944-11953, 10.1021/es502204x, 2014.
- 660 Guenther, A., Hewitt, C. N., Erickson, D., Fall, R., Geron, C., Graedel, T., Harley, P., Klinger, L., Lerdau, M., and McKay, W.: A global model of natural volatile organic compound emissions, *Journal of Geophysical Research: Atmospheres* (1984–2012), 100, 8873-8892, 1995.
- Guenther, A., Karl, T., Harley, P., Wiedinmyer, C., Palmer, P., and Geron, C.: Estimates of global terrestrial isoprene emissions using MEGAN (Model of Emissions of Gases and Aerosols from Nature), *Atmos Chem Phys*, 6, 3181-3210, 2006.
- 665 Hallquist, M., Wenger, J. C., Baltensperger, U., Rudich, Y., Simpson, D., Claeys, M., Dommen, J., Donahue, N. M., George, C., Goldstein, A. H., Hamilton, J. F., Herrmann, H., Hoffmann, T., Iinuma, Y., Jang, M., Jenkin, M. E., Jimenez, J. L., Kiendler-Scharr, A., Maenhaut, W., McFiggans, G., Mentel, T. F., Monod, A., Prévôt, A. S. H., Seinfeld, J. H., Surratt, J. D., Szmigielski, R., and Wildt, J.: The formation, properties and impact of secondary organic aerosol: current and emerging issues, *Atmos. Chem. Phys.*, 9, 5155-5236, 10.5194/acp-9-5155-2009, 2009.
- 670 He, Q., Tomaz, S., Li, C., Zhu, M., Meidan, D., Riva, M., Laskin, A., Brown, S. S., George, C., Wang, X., and Rudich, Y.: Optical Properties of Secondary Organic Aerosol Produced by Nitrate Radical Oxidation of Biogenic Volatile Organic Compounds, *Environmental Science & Technology*, 55, 2878-2889, 10.1021/acs.est.0c06838, 2021.
- Henry, K. M., and Donahue, N. M.: Photochemical Aging of α -Pinene Secondary Organic Aerosol: Effects of OH Radical Sources and Photolysis, *The Journal of Physical Chemistry A*, 116, 5932-5940, 10.1021/jp210288s, 2012.
- 675 Hoyle, C. R., Berntsen, T., Myhre, G., and Isaksen, I. S. A.: Secondary organic aerosol in the global aerosol – chemical transport model Oslo CTM2, *Atmos. Chem. Phys.*, 7, 5675-5694, 10.5194/acp-7-5675-2007, 2007.

- Huang, W., Saathoff, H., Pajunoja, A., Shen, X., Naumann, K. H., Wagner, R., Virtanen, A., Leisner, T., and Mohr, C.: α -Pinene secondary organic aerosol at low temperature: chemical composition and implications for particle viscosity, *Atmos. Chem. Phys.*, 18, 2883-2898, 10.5194/acp-18-2883-2018, 2018.
- 680 Isaacman-VanWertz, G., and Aumont, B.: Impact of organic molecular structure on the estimation of atmospherically relevant physicochemical parameters, *Atmos. Chem. Phys.*, 21, 6541-6563, 10.5194/acp-21-6541-2021, 2021.
- Jaoui, M., Kleindienst, T. E., Docherty, K. S., Lewandowski, M., and Offenberg, J. H.: Secondary organic aerosol formation from the oxidation of a series of sesquiterpenes: α -cedrene, β -caryophyllene, α -humulene and α -farnesene with O₃, OH and NO₃ radicals, *Environmental Chemistry*, 10, 178-193, <https://doi.org/10.1071/EN13025>, 2013.
- 685 Jenkin, M. E., Saunders, S. M., and Pilling, M. J.: The tropospheric degradation of volatile organic compounds: a protocol for mechanism development, *Atmospheric Environment*, 31, 81-104, [https://doi.org/10.1016/S1352-2310\(96\)00105-7](https://doi.org/10.1016/S1352-2310(96)00105-7), 1997.
- Kiendler-Scharr, A., Mensah, A. A., Friese, E., Topping, D., Nemitz, E., Prevot, A. S. H., Äijälä, M., Allan, J., Canonaco, F., Canagaratna, M., Carbone, S., Crippa, M., Dall'Osto, M., Day, D. A., De Carlo, P., Di Marco, C. F., Elbern, H., Eriksson, A., Freney, E., Hao, L., Herrmann, H., Hildebrandt, L., Hillamo, R., Jimenez, J. L., Laaksonen, A., McFiggans, G., Mohr, C., O'Dowd, C., Otjes, R., Ovadnevaite, J., Pandis, S. N., Poulain, L., Schlag, P., Sellegri, K., Swietlicki, E., Tiitta, P., Vermeulen, A., Wahner, A., Worsnop, D., and Wu, H.-C.: Ubiquity of organic nitrates from nighttime chemistry in the European submicron aerosol, *Geophysical Research Letters*, 43, 7735-7744, <https://doi.org/10.1002/2016GL069239>, 2016.
- 690 Krapf, M., El Haddad, I., Bruns, Emily A., Molteni, U., Daellenbach, Kaspar R., Prévôt, André S. H., Baltensperger, U., and Dommen, J.: Labile Peroxides in Secondary Organic Aerosol, *Chem*, 1, 603-616, <https://doi.org/10.1016/j.chempr.2016.09.007>, 2016.
- 695 Lee, B. H., Lopez-Hilfiker, F. D., Mohr, C., Kurtén, T., Worsnop, D. R., and Thornton, J. A.: An Iodide-Adduct High-Resolution Time-of-Flight Chemical-Ionization Mass Spectrometer: Application to Atmospheric Inorganic and Organic Compounds, *Environmental Science & Technology*, 48, 6309-6317, 10.1021/es500362a, 2014.
- 700 Lee, B. H., Mohr, C., Lopez-Hilfiker, F. D., Lutz, A., Hallquist, M., Lee, L., Romer, P., Cohen, R. C., Iyer, S., Kurtén, T., Hu, W., Day, D. A., Campuzano-Jost, P., Jimenez, J. L., Xu, L., Ng, N. L., Guo, H., Weber, R. J., Wild, R. J., Brown, S. S., Koss, A., de Gouw, J., Olson, K., Goldstein, A. H., Seco, R., Kim, S., McAvey, K., Shepson, P. B., Starn, T., Baumann, K., Edgerton, E. S., Liu, J., Shilling, J. E., Miller, D. O., Brune, W., Schobesberger, S., D'Ambro, E. L., and Thornton, J. A.: Highly functionalized organic nitrates in the southeast United States: Contribution to secondary organic aerosol and reactive nitrogen budgets, *Proceedings of the National Academy of Sciences*, 113, 1516-1521, 10.1073/pnas.1508108113, 2016.
- 705 Li, Y., Pöschl, U., and Shiraiwa, M.: Molecular corridors and parameterizations of volatility in the chemical evolution of organic aerosols, *Atmos. Chem. Phys.*, 16, 3327-3344, 10.5194/acp-16-3327-2016, 2016.
- Liu, X., Day, D. A., Krechmer, J. E., Brown, W., Peng, Z., Ziemann, P. J., and Jimenez, J. L.: Direct measurements of semi-volatile organic compound dynamics show near-unity mass accommodation coefficients for diverse aerosols, *Communications Chemistry*, 2, 98, 10.1038/s42004-019-0200-x, 2019.
- 710 Lopez-Hilfiker, F. D., Mohr, C., Ehn, M., Rubach, F., Kleist, E., Wildt, J., Mentel, T. F., Lutz, A., Hallquist, M., Worsnop, D., and Thornton, J. A.: A novel method for online analysis of gas and particle composition: description and evaluation of a Filter Inlet for Gases and AEROSols (FIGAERO), *Atmos. Meas. Tech.*, 7, 983-1001, 10.5194/amt-7-983-2014, 2014.
- Lopez-Hilfiker, F. D., Pospisilova, V., Huang, W., Kalberer, M., Mohr, C., Stefenelli, G., Thornton, J. A., Baltensperger, U., Prevot, A. S. H., and Slowik, J. G.: An extractive electrospray ionization time-of-flight mass spectrometer (EESI-TOF) for online measurement of atmospheric aerosol particles, *Atmos. Meas. Tech.*, 12, 4867-4886, 10.5194/amt-12-4867-2019, 2019.
- 715 Mang, S. A., Henricksen, D. K., Bateman, A. P., Andersen, M. P. S., Blake, D. R., and Nizkorodov, S. A.: Contribution of Carbonyl Photochemistry to Aging of Atmospheric Secondary Organic Aerosol, *The Journal of Physical Chemistry A*, 112, 8337-8344, 10.1021/jp804376c, 2008.
- Mohr, C., Thornton, J. A., Heitto, A., Lopez-Hilfiker, F. D., Lutz, A., Riipinen, I., Hong, J., Donahue, N. M., Hallquist, M., Petäjä, T., Kulmala, M., and Yli-Juuti, T.: Molecular identification of organic vapors driving atmospheric nanoparticle growth, *Nature Communications*, 10, 4442, 10.1038/s41467-019-12473-2, 2019.
- Müller, J. F., Peeters, J., and Stavrou, T.: Fast photolysis of carbonyl nitrates from isoprene, *Atmos. Chem. Phys.*, 14, 2497-2508, 10.5194/acp-14-2497-2014, 2014.
- Nah, T., Sanchez, J., Boyd, C. M., and Ng, N. L.: Photochemical Aging of α -pinene and β -pinene Secondary Organic Aerosol formed from Nitrate Radical Oxidation, *Environmental Science & Technology*, 50, 222-231, 10.1021/acs.est.5b04594, 2016.
- 725 Nakayama, T., Sato, K., Tsuge, M., Imamura, T., and Matsumi, Y.: Complex refractive index of secondary organic aerosol generated from isoprene/NO_x photooxidation in the presence and absence of SO₂, *Journal of Geophysical Research: Atmospheres*, 120, 7777-7787, <https://doi.org/10.1002/2015JD023522>, 2015.
- 730 Ng, N. L., Kwan, A. J., Surratt, J. D., Chan, A. W. H., Chhabra, P. S., Sorooshian, A., Pye, H. O. T., Crounse, J. D., Wennberg, P. O., Flagan, R. C., and Seinfeld, J. H.: Secondary organic aerosol (SOA) formation from reaction of isoprene with nitrate radicals (NO₃), *Atmos. Chem. Phys.*, 8, 4117-4140, 10.5194/acp-8-4117-2008, 2008.
- O'Meara, S., Booth, A. M., Barley, M. H., Topping, D., and McFiggans, G.: An assessment of vapour pressure estimation methods, *Physical Chemistry Chemical Physics*, 16, 19453-19469, 10.1039/C4CP00857J, 2014.

- O'Brien, R. E., and Kröll, J. H.: Photolytic Aging of Secondary Organic Aerosol: Evidence for a Substantial Photo-Recalcitrant Fraction, *The Journal of Physical Chemistry Letters*, 10, 4003-4009, 10.1021/acs.jpcclett.9b01417, 2019.
- 735 Pan, X., Underwood, J. S., Xing, J. H., Mang, S. A., and Nizkorodov, S. A.: Photodegradation of secondary organic aerosol generated from limonene oxidation by ozone studied with chemical ionization mass spectrometry, *Atmos. Chem. Phys.*, 9, 3851-3865, 10.5194/acp-9-3851-2009, 2009.
- Pankow, J. F., and Asher, W. E.: SIMPOL.1: a simple group contribution method for predicting vapor pressures and enthalpies of vaporization of multifunctional organic compounds, *Atmos. Chem. Phys.*, 8, 2773-2796, 10.5194/acp-8-2773-2008, 2008.
- 740 Peng, C., Wang, W., Li, K., Li, J., Zhou, L., Wang, L., and Ge, M.: The Optical Properties of Limonene Secondary Organic Aerosols: The Role of NO₃, OH, and O₃ in the Oxidation Processes, *Journal of Geophysical Research: Atmospheres*, 123, 3292-3303, <https://doi.org/10.1002/2017JD028090>, 2018.
- 745 Peräkylä, O., Riva, M., Heikkinen, L., Quéléver, L., Roldin, P., and Ehn, M.: Experimental investigation into the volatilities of highly oxygenated organic molecules (HOMs), *Atmos. Chem. Phys.*, 20, 649-669, 10.5194/acp-20-649-2020, 2020.
- Perring, A. E., Pusede, S. E., and Cohen, R. C.: An Observational Perspective on the Atmospheric Impacts of Alkyl and Multifunctional Nitrates on Ozone and Secondary Organic Aerosol, *Chemical Reviews*, 113, 5848-5870, 10.1021/cr300520x, 2013.
- Platt, S. M., El Haddad, I., Zardini, A. A., Clairotte, M., Astorga, C., Wolf, R., Slowik, J. G., Temime-Roussel, B., Marchand, N., Ježek, I., Drinovec, L., Močnik, G., Möhler, O., Richter, R., Barmet, P., Bianchi, F., Baltensperger, U., and Prévôt, A. S. H.: Secondary organic aerosol formation from gasoline vehicle emissions in a new mobile environmental reaction chamber, *Atmos. Chem. Phys.*, 13, 9141-9158, 10.5194/acp-13-9141-2013, 2013.
- 750 Pospisilova, V., Lopez-Hilfiker, F. D., Bell, D. M., El Haddad, I., Mohr, C., Huang, W., Heikkinen, L., Xiao, M., Dommen, J., Prevot, A. S. H., Baltensperger, U., and Slowik, J. G.: On the fate of oxygenated organic molecules in atmospheric aerosol particles, *Science Advances*, 6, eaax8922, 10.1126/sciadv.aax8922, 2020.
- 755 Presto, A. A., Huff Hartz, K. E., and Donahue, N. M.: Secondary Organic Aerosol Production from Terpene Ozonolysis. 1. Effect of UV Radiation, *Environmental Science & Technology*, 39, 7036-7045, 10.1021/es050174m, 2005.
- Pye, H. O. T., Chan, A. W. H., Barkley, M. P., and Seinfeld, J. H.: Global modeling of organic aerosol: the importance of reactive nitrogen (NO_x and NO₃), *Atmos. Chem. Phys.*, 10, 11261-11276, 10.5194/acp-10-11261-2010, 2010.
- 760 Pye, H. O. T., Luecken, D. J., Xu, L., Boyd, C. M., Ng, N. L., Baker, K. R., Ayres, B. R., Bash, J. O., Baumann, K., Carter, W. P. L., Edgerton, E., Fry, J. L., Hutzell, W. T., Schwede, D. B., and Shepson, P. B.: Modeling the Current and Future Roles of Particulate Organic Nitrates in the Southeastern United States, *Environmental Science & Technology*, 49, 14195-14203, 10.1021/acs.est.5b03738, 2015.
- Riipinen, I., Pierce, J. R., Donahue, N. M., and Pandis, S. N.: Equilibration time scales of organic aerosol inside thermodenuders: Evaporation kinetics versus thermodynamics, *Atmospheric Environment*, 44, 597-607, <https://doi.org/10.1016/j.atmosenv.2009.11.022>, 2010.
- 765 Rollins, A. W., Kiendler-Scharr, A., Fry, J. L., Brauers, T., Brown, S. S., Dorn, H. P., Dubé, W. P., Fuchs, H., Mensah, A., Mentel, T. F., Rohrer, F., Tillmann, R., Wegener, R., Wooldridge, P. J., and Cohen, R. C.: Isoprene oxidation by nitrate radical: alkyl nitrate and secondary organic aerosol yields, *Atmos. Chem. Phys.*, 9, 6685-6703, 10.5194/acp-9-6685-2009, 2009.
- Schobesberger, S., D'Ambro, E. L., Lopez-Hilfiker, F. D., Mohr, C., and Thornton, J. A.: A model framework to retrieve thermodynamic and kinetic properties of organic aerosol from composition-resolved thermal desorption measurements, *Atmos. Chem. Phys.*, 18, 14757-14785, 10.5194/acp-18-14757-2018, 2018.
- 770 Shrivastava, M., Cappa, C. D., Fan, J., Goldstein, A. H., Guenther, A. B., Jimenez, J. L., Kuang, C., Laskin, A., Martin, S. T., Ng, N. L., Petaja, T., Pierce, J. R., Rasch, P. J., Roldin, P., Seinfeld, J. H., Shilling, J., Smith, J. N., Thornton, J. A., Volkamer, R., Wang, J., Worsnop, D. R., Zaveri, R. A., Zelenyuk, A., and Zhang, Q.: Recent advances in understanding secondary organic aerosol: Implications for global climate forcing, *Reviews of Geophysics*, 55, 509-559, <https://doi.org/10.1002/2016RG000540>, 2017.
- 775 Suarez-Bertoa, R., Picquet-Varrault, B., Tamas, W., Pangui, E., and Doussin, J. F.: Atmospheric Fate of a Series of Carbonyl Nitrates: Photolysis Frequencies and OH-Oxidation Rate Constants, *Environmental Science & Technology*, 46, 12502-12509, 10.1021/es302613x, 2012.
- Surratt, J. D., Murphy, S. M., Kröll, J. H., Ng, N. L., Hildebrandt, L., Sorooshian, A., Szmigielski, R., Vermeylen, R., Maenhaut, W., Claeys, M., Flagan, R. C., and Seinfeld, J. H.: Chemical Composition of Secondary Organic Aerosol Formed from the Photooxidation of Isoprene, *The Journal of Physical Chemistry A*, 110, 9665-9690, 10.1021/jp061734m, 2006.
- 780 Takeuchi, M., and Ng, N. L.: Chemical composition and hydrolysis of organic nitrate aerosol formed from hydroxyl and nitrate radical oxidation of α -pinene and β -pinene, *Atmos. Chem. Phys.*, 19, 12749-12766, 10.5194/acp-19-12749-2019, 2019.
- Thornton, J. A., Mohr, C., Schobesberger, S., D'Ambro, E. L., Lee, B. H., and Lopez-Hilfiker, F. D.: Evaluating Organic Aerosol Sources and Evolution with a Combined Molecular Composition and Volatility Framework Using the Filter Inlet for Gases and Aerosols (FIGAERO), *Accounts of Chemical Research*, 53, 1415-1426, 10.1021/acs.accounts.0c00259, 2020.
- 785 Tritscher, T., Dommen, J., DeCarlo, P. F., Gysel, M., Barmet, P. B., Praplan, A. P., Weingartner, E., Prévôt, A. S. H., Riipinen, I., Donahue, N. M., and Baltensperger, U.: Volatility and hygroscopicity of aging secondary organic aerosol in a smog chamber, *Atmos. Chem. Phys.*, 11, 11477-11496, 10.5194/acp-11-11477-2011, 2011.

- 790 Tröstl, J., Chuang, W. K., Gordon, H., Heinritzi, M., Yan, C., Molteni, U., Ahlm, L., Frege, C., Bianchi, F., Wagner, R., Simon, M., Lehtipalo, K., Williamson, C., Craven, J. S., Duplissy, J., Adamov, A., Almeida, J., Bernhammer, A.-K., Breitenlechner, M., Brilke, S., Dias, A., Ehrhart, S., Flagan, R. C., Franchin, A., Fuchs, C., Guida, R., Gysel, M., Hansel, A., Hoyle, C. R., Jokinen, T., Junninen, H., Kangasluoma, J., Keskinen, H., Kim, J., Krapf, M., Kürten, A., Laaksonen, A., Lawler, M., Leiminger, M., Mathot, S., Möhler, O., Nieminen, T., Onnela, A., Petäjä, T., Piel, F. M., Miettinen, P., Rissanen, M. P., Rondo, L., Sarnela, N., Schobesberger, S., Sengupta, K., Sipilä, M., Smith, J. N., Steiner, G., Tomè, A., Virtanen, A., Wagner, A. C., Weingartner, E., Wimmer, D., Winkler, P. M., Ye, P., Carslaw, K. S., Curtius, J., Dommen, J., Kirkby, J., Kulmala, M., Riipinen, I., Worsnop, D. R., Donahue, N. M., and Baltensperger, U.: The role of low-volatility organic compounds in initial particle growth in the atmosphere, *Nature*, 533, 527-531, 10.1038/nature18271, 2016.
- Vaden, T. D., Imre, D., Beránek, J., Shrivastava, M., and Zelenyuk, A.: Evaporation kinetics and phase of laboratory and ambient secondary organic aerosol, *Proceedings of the National Academy of Sciences*, 108, 2190-2195, 10.1073/pnas.1013391108, 2011.
- 800 Walser, M. L., Park, J., Gomez, A. L., Russell, A. R., and Nizkorodov, S. A.: Photochemical Aging of Secondary Organic Aerosol Particles Generated from the Oxidation of d-Limonene, *The Journal of Physical Chemistry A*, 111, 1907-1913, 10.1021/jp066293l, 2007.
- Wolfe, G. M., Marvin, M. R., Roberts, S. J., Travis, K. R., and Liao, J.: The Framework for 0-D Atmospheric Modeling (FOAM) v3.1, *Geosci. Model Dev.*, 9, 3309-3319, 10.5194/gmd-9-3309-2016, 2016.
- 805 Wong, J. P. S., Zhou, S., and Abbatt, J. P. D.: Changes in Secondary Organic Aerosol Composition and Mass due to Photolysis: Relative Humidity Dependence, *The Journal of Physical Chemistry A*, 119, 4309-4316, 10.1021/jp506898c, 2015.
- Wu, R., Vereecken, L., Tsiligiannis, E., Kang, S., Albrecht, S. R., Hantschke, L., Zhao, D., Novelli, A., Fuchs, H., Tillmann, R., Hohaus, T., Carlsson, P. T. M., Shenolikar, J., Bernard, F., Crowley, J. N., Fry, J. L., Brownwood, B., Thornton, J. A., Brown, S. S., Kiendler-Scharr, A., Wahner, A., Hallquist, M., and Mentel, T. F.: Molecular composition and volatility of multi-generation products formed from isoprene oxidation by nitrate radical, *Atmos. Chem. Phys. Discuss.*, 2020, 1-37, 10.5194/acp-2020-1180, 2020.
- 810 Wu, R., Vereecken, L., Tsiligiannis, E., Kang, S., Albrecht, S. R., Hantschke, L., Zhao, D., Novelli, A., Fuchs, H., Tillmann, R., Hohaus, T., Carlsson, P. T. M., Shenolikar, J., Bernard, F., Crowley, J. N., Fry, J. L., Brownwood, B., Thornton, J. A., Brown, S. S., Kiendler-Scharr, A., Wahner, A., Hallquist, M., and Mentel, T. F.: Molecular composition and volatility of multi-generation products formed from isoprene oxidation by nitrate radical, *Atmos. Chem. Phys.*, 21, 10799-10824, 10.5194/acp-21-10799-2021, 2021.
- 815 Zare, A., Romer, P. S., Nguyen, T., Keutsch, F. N., Skog, K., and Cohen, R. C.: A comprehensive organic nitrate chemistry: insights into the lifetime of atmospheric organic nitrates, *Atmos. Chem. Phys.*, 18, 15419-15436, 10.5194/acp-18-15419-2018, 2018.
- Zawadowicz, M. A., Lee, B. H., Shrivastava, M., Zelenyuk, A., Zaveri, R. A., Flynn, C., Thornton, J. A., and Shilling, J. E.: Photolysis Controls Atmospheric Budgets of Biogenic Secondary Organic Aerosol, *Environmental Science & Technology*, 54, 3861-3870, 10.1021/acs.est.9b07051, 2020.
- 820 Zhao, D., Pullinen, I., Fuchs, H., Schrade, S., Wu, R., Acir, I. H., Tillmann, R., Rohrer, F., Wildt, J., Guo, Y., Kiendler-Scharr, A., Wahner, A., Kang, S., Vereecken, L., and Mentel, T. F.: Highly oxygenated organic molecules (HOM) formation in the isoprene oxidation by NO₃ radical, *Atmos. Chem. Phys. Discuss.*, 2020, 1-28, 10.5194/acp-2020-1178, 2020.
- 825 Zhao, Z., Tolentino, R., Lee, J., Vuong, A., Yang, X., and Zhang, H.: Interfacial Dimerization by Organic Radical Reactions during Heterogeneous Oxidative Aging of Oxygenated Organic Aerosols, *The Journal of Physical Chemistry A*, 123, 10782-10792, 10.1021/acs.jpca.9b10779, 2019.

Supporting information

S1 Data analysis of FIGAERO-CIMS

Data from the FIGAERO-CIMS was analysed with Tofware (Aerodyne Research, Inc. and Tofwerk AG) and Igor Pro (WaveMetrics Inc.). The initial mass calibration was conducted on I^- , IH_2O^- , $IHNO_3^-$, and I_3^- . In addition, the chemical composition of the 2–3 major dimer peaks were confirmed by the compounds measured simultaneously by the EESI-TOF, and these clearly identified ions were used as mass calibrants as well for the mass range higher than 400 Th. After processing the high resolution (HR) ion fits, the subsequent treatment of the processed HR data was performed using code written with MATLAB for checking signal to noise ratio, integrating thermogram data, etc.

S1.1 Background subtraction

For each experiment, one particle blank (zero sampling time + normal heating) was performed during dark aging. Because the background signal varies for each filters/experiment, when subtracting the background from the signals of normal filters, the integrated area of the particle blank from the same experiment was scaled up/down with a scaling factor. This factor was determined by comparing the detected signals of the last 1min of “temp soak” of the normal heating to the detected signals of the last 1min of “temp soak” of the zero heating) (Fig. S1).

S1.2 Impact of thermal decomposition on FIGAERO particle phase measurement

For the FIGAERO inlet, the artifacts associated with thermal decomposition have been were discussed in many previous studies (Lopez-Hilfiker et al., 2015; D'Ambro et al., 2019; Stark et al., 2017). We corrected the impact of thermal decomposition for further analysis on the chemical composition and temperature at maximum desorption rate (T_{max}) with the following steps:

- (1) If the thermogram of a compound exhibited multiple peaks (Fig. S2a), T_{max} was determined based on the first peak, and the peak area was integrated only for the first peak.
- (2) If the thermogram of a compound was monomodal, but T_{max} was “too high” based on its chemical composition (e.g., $C_5H_{10}N_2O_9$ has a similar T_{max} as that of $C_{10}H_{17}N_3O_{13}$, Fig. S2b), this compound was excluded from the analysis of the chemical composition.

Fig. S3 shows thermal fragmentation to be a minor issue in our study. Most of the peaks in the three systems do not have “shoulders” or “plateaus”. In addition, for almost all compounds in the isoprene and α -pinene systems and the monomers in the β -caryophyllene system, the signals in the temperature range higher than 120 °C where dehydration or decarboxylation reactions are expected to occur

(Buchholz et al., 2020; Stark et al., 2017) are relatively low. There are a few exceptions with bi-modal thermograms (Fig. S3c, blue lines), which were corrected for as described above. Regarding the dimers from the β -caryophyllene system (Figure S3d), there are a few compounds with significant tailings. However, their molecular formulae do not correspond to thermal decomposition products of major dimers (e.g. dehydration products with $m/z - 18.015$ compared to the parent compounds), but the tailings might rather be signal from isomers of these major dimers.

S1.3 Uncertainties in the gas-phase measurement

The uncertainties in the gas-phase measurement due to the changing ratios of I/NO_3^- were tested after Exp. 2 (isoprene + NO_3^-). The total gas phase flow for the FIGAERO-CIMS was 5 L min^{-1} and it was partly replaced by 1.5, 3.0, 4.0 L min^{-1} N_2 with keeping the total flow constant, causing $I/NO_3^- = 0.09$ (no dilution), 0.14, 0.28 and 1.6. In Fig. S3S4, three major gas-phase compounds $C_5H_{10}IN_2O_8^-$, $C_5H_9INO_6^-$, $C_5H_9IN_3O_{10}^-$ were chosen and their normalized signals (to the signals measured without dilution and with the consideration of dilution rates) were compared. The normalized signal didn't change significantly with decreasing I/NO_3^- as long as I/NO_3^- was higher than ~ 0.3 , but it decreased about 20–40% when I/NO_3^- decreased further and was close to 0.1.

S2 Size dependence of light absorption

In Fig. S4S5, we simulated the difference between the mass absorption efficiency ($\text{m}^2 \text{ g}^{-1}$, MAE) at wavelength = 350 nm of larger particles (diameter = 300 nm) versus smaller particles (diameter = 100 nm) as a function of an imaginary part of the refractive index using MiePlot, based on the equations found elsewhere (Bohren and Huffman, 1998). The imaginary part of the refractive index corresponds to species that absorb light. With a value of 0.001, the MAE of 300 nm particles is 1.7 times higher than the MAE of 100 nm particles. Although no direct measurement of the imaginary part of the refractive index was conducted in this study, based on a summary of different SOA systems by (Nakayama et al., 2015) and the study of He et al. (2021), a value between 0.001 and 0.01 could be expected for biogenic VOC species studied here.

SI Figures

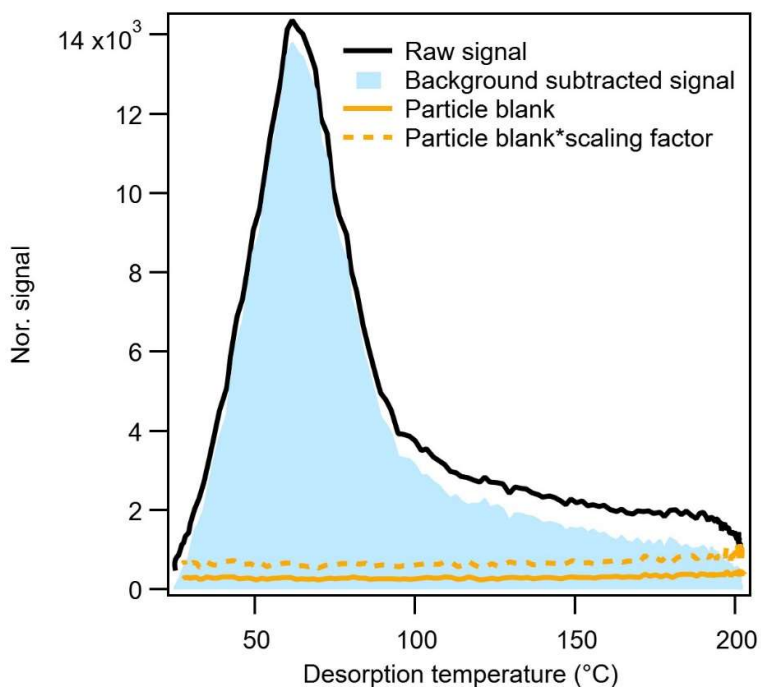


Fig. S1 Thermogram background subtraction for a typical compound $C_{10}H_{16}N_2O_{10}$ from Exp.2: isoprene + NO_3 .

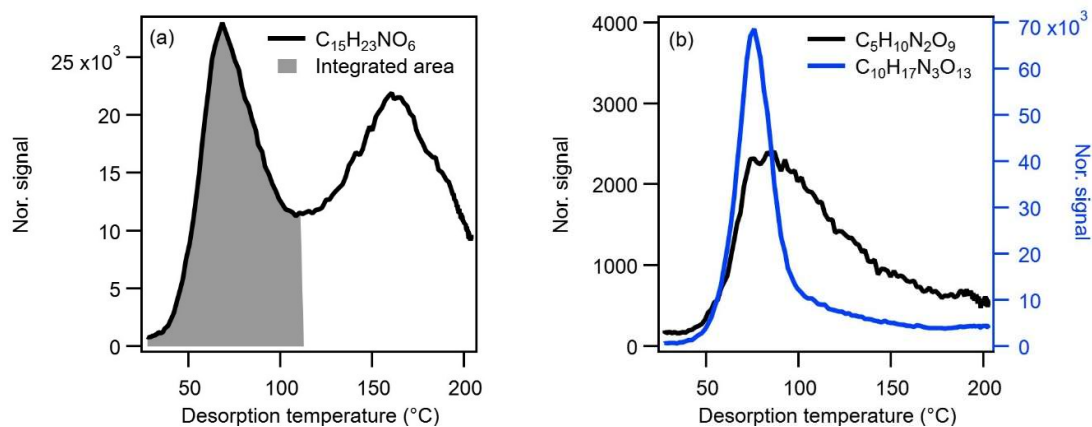


Fig. S2 (a) Thermogram of $C_{15}H_{23}NO_6$, the shaded area represents the integrated area. (b) Thermogram of $C_5H_{10}N_2O_9$, compared to that of $C_{10}H_{17}N_3O_{13}$ from a filter sample of Exp. 1: isoprene + NO_3 .

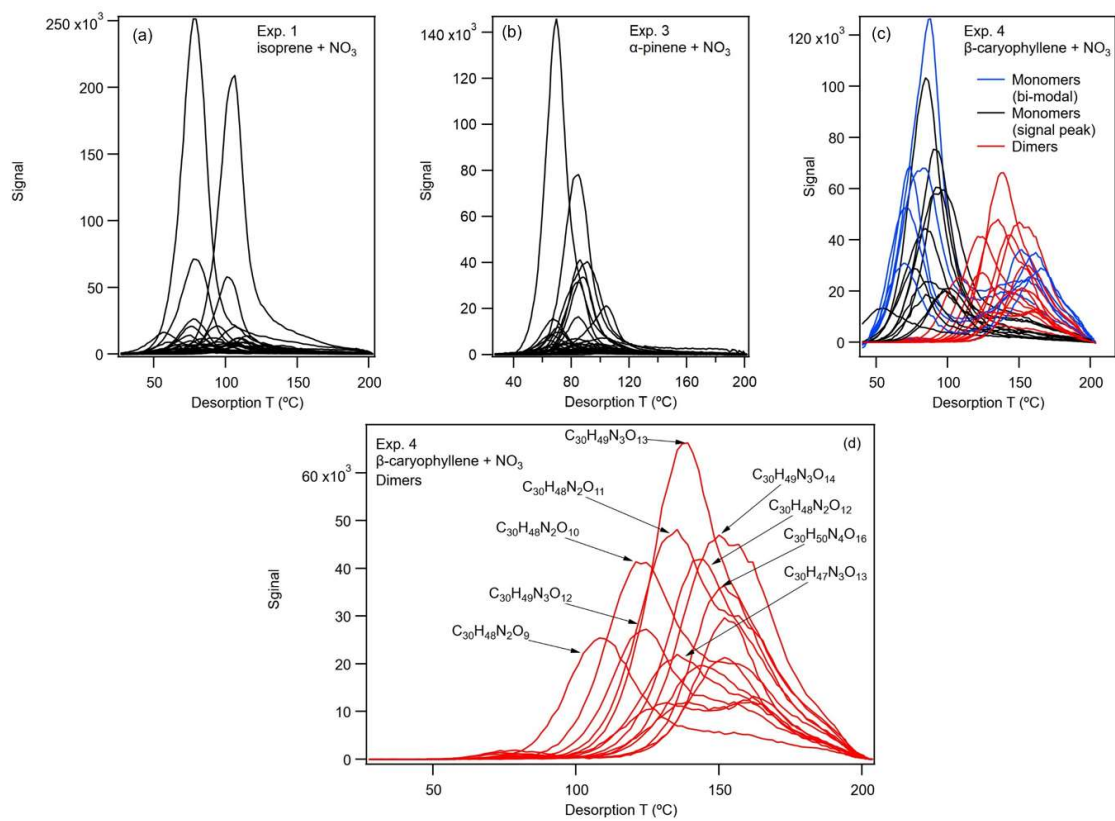


Fig. S3 Thermograms of top 30 (signal) compounds of the SOA from (a) Exp.1, (b) Exp. 3 and (c) Exp. 4 and (d) major dimers from Exp. 4.

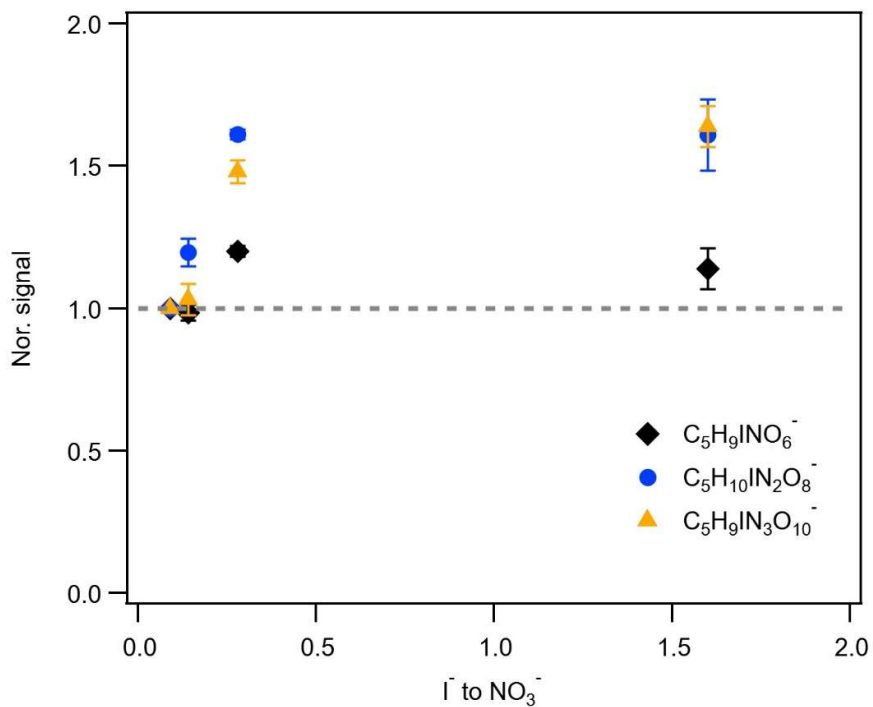


Fig. S3-S4 Normalized signal of three major compounds in the gas phase from Exp. 2: isoprene + NO_3 as a function of \bar{I}/NO_3^- ratio.

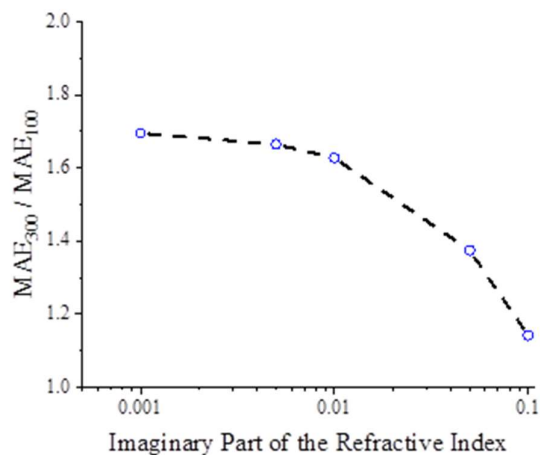


Fig. S4-S5 Mass absorption efficiency (MAE) of 300 nm particles versus that of 100 nm particles at wavelength of 300 nm, as a function of imaginary part of the refractive index.

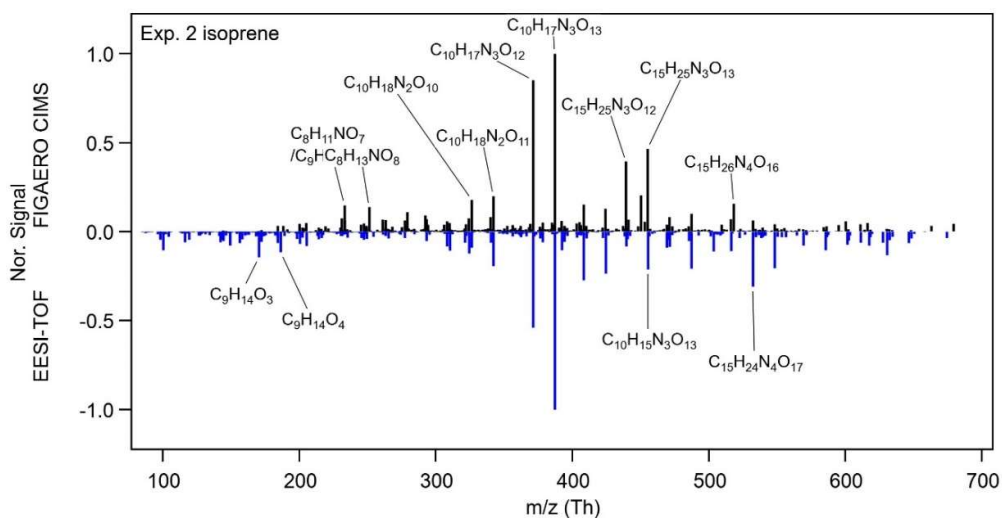


Fig. S5-S6 FIGAERO-CIMS (positive axis) and EESI-TOF (negative axis) mass spectra of particle phase $C_xH_yO_zN_{0-4}$ formed during Exp. 2: isoprene + NO_3 shortly before photolysis. For the FIGAERO-CIMS, the last filter before photolysis is chosen. The EESI-TOF mass spectra are averaged mass spectra during the same sampling time as that of FIGAERO-CIMS. All mass spectra are normalized to the corresponding maximal signal.

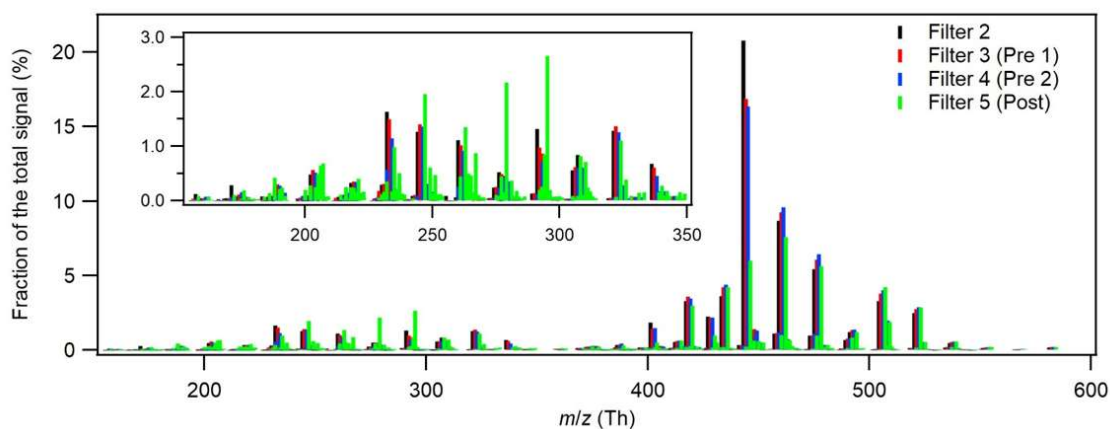


Fig. S7 Mass spectra of four filter collected during dark aging and photolysis in Exp.3.

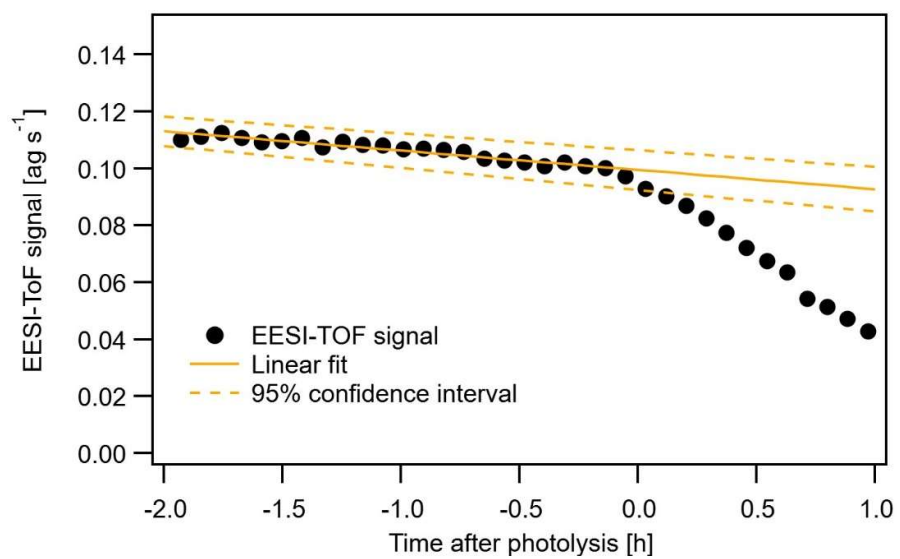


Fig. S86 Time series of $C_{10}H_{17}N_3O_{13}$ measured by the EESI-TOF and linear fit (with 95% confidence interval) of the 2 h pre-photolysis data points.

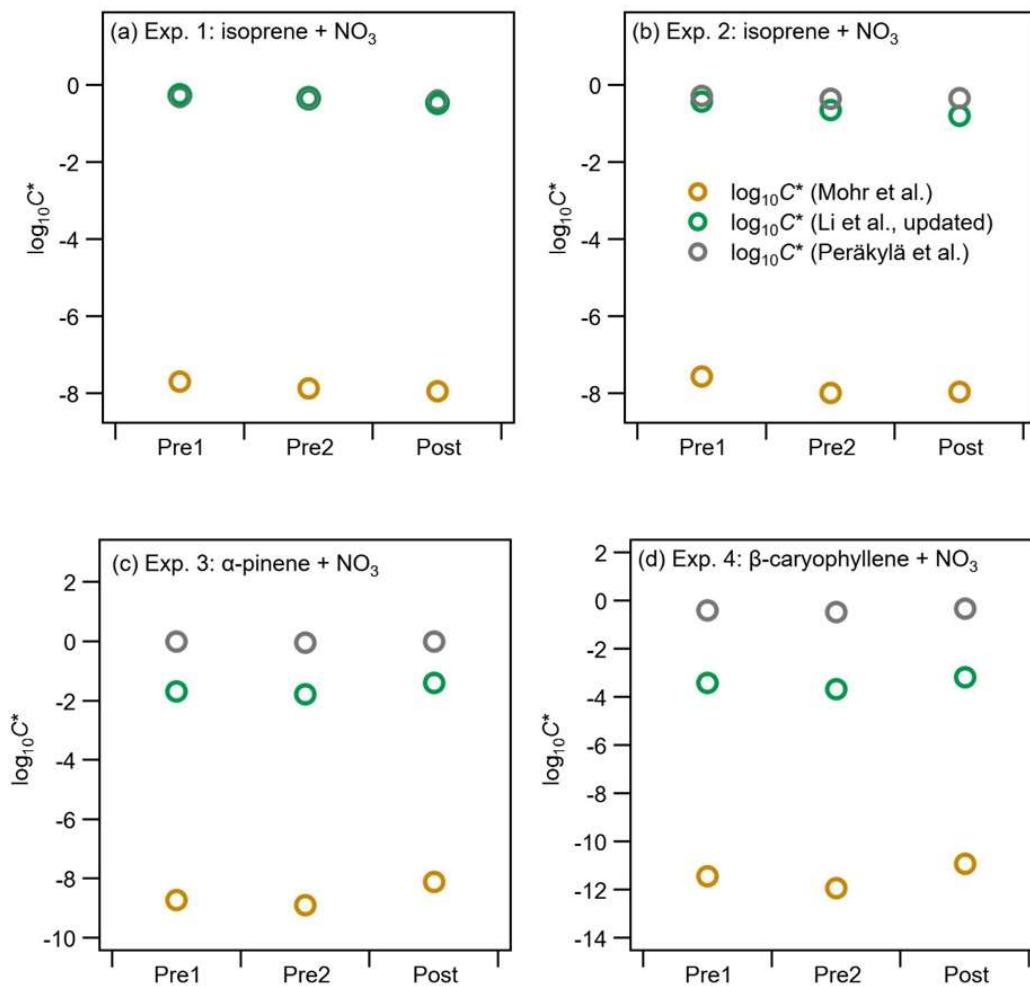


Fig. S97 Bulk $\log_{10}C^*$ calculated by Mohr et al. (2019), Li et al. (2016) (updated by Isaacman-VanWertz and Aumont (2021)), Peräkylä et al. (2020) for the three filters (Pre 1, Pre 2 and Post) from all experiments.

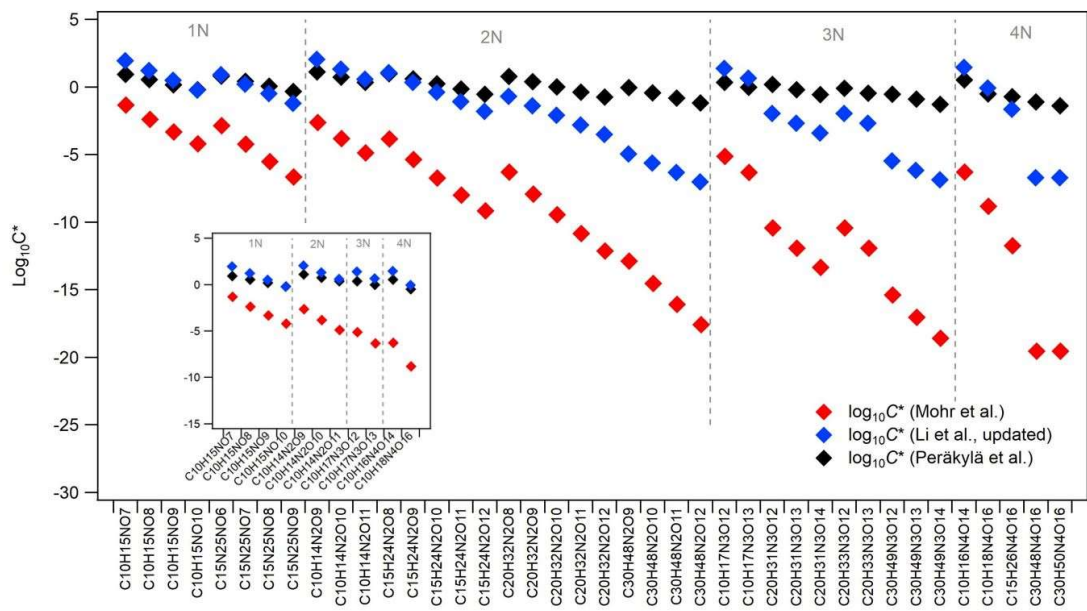


Fig. S10 $\text{log}_{10} C^*$ based on the parameterizations of Mohr et al. (2019), Li et al. (2016) (updated by Isaacman-VanWertz and Aumont (2021)), and Peräkylä et al. (2020) of major compounds with 1 – 4 N from all three systems. In the small panel, only C10 compounds are compared.

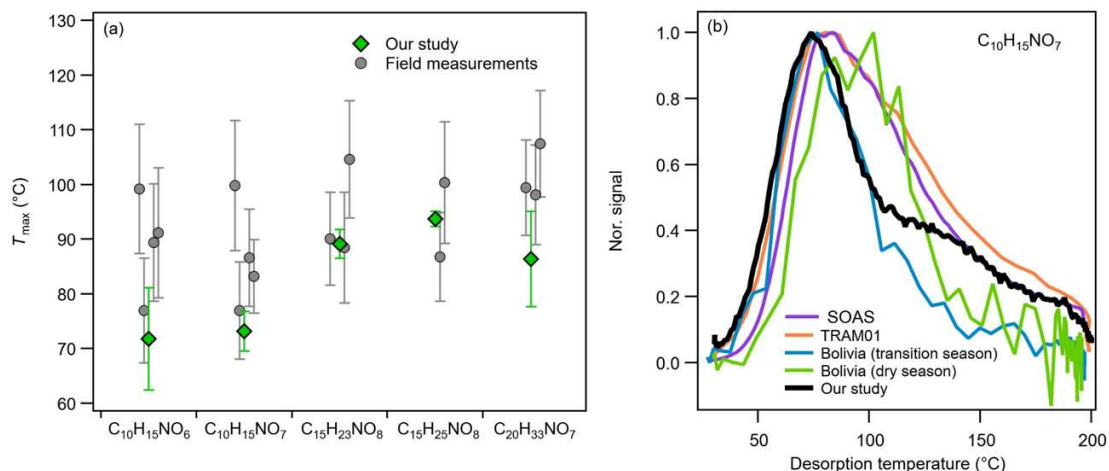


Fig. S118 (a) Comparison between the average T_{max} with standard deviation of $C_{10}H_{15}NO_{6,7}$, $C_{15}H_{23,25}NO_8$ and $C_{20}H_{33}NO_7$ from our study (mass loadings between ~ 0.3 and $\sim 3 \mu\text{g}$) including both dark aging and photolysis periods and three field campaigns: SOAS (Lopez-Hilfiker et al., 2016), TRAM01 (Huang et al., 2019) and the Bolivia campaign (during both transition season and dry season, Huang et al. in preparation). (b) Average thermograms of $C_{10}H_{15}NO_7$ from our study and the field campaigns. The mean mass loading was 0.33 ± 0.22 , 1.45 ± 0.95 , 0.07 ± 0.06 and $0.21 \pm 0.16 \mu\text{g}$, and the time of ramping the temperature of the nitrogen flow from ambient temperature up to 200 °C was 20, 15, 15 and 15 min for SOAS, TRAM01, Bolivia (transition season) and Bolivia (dry season), respectively.

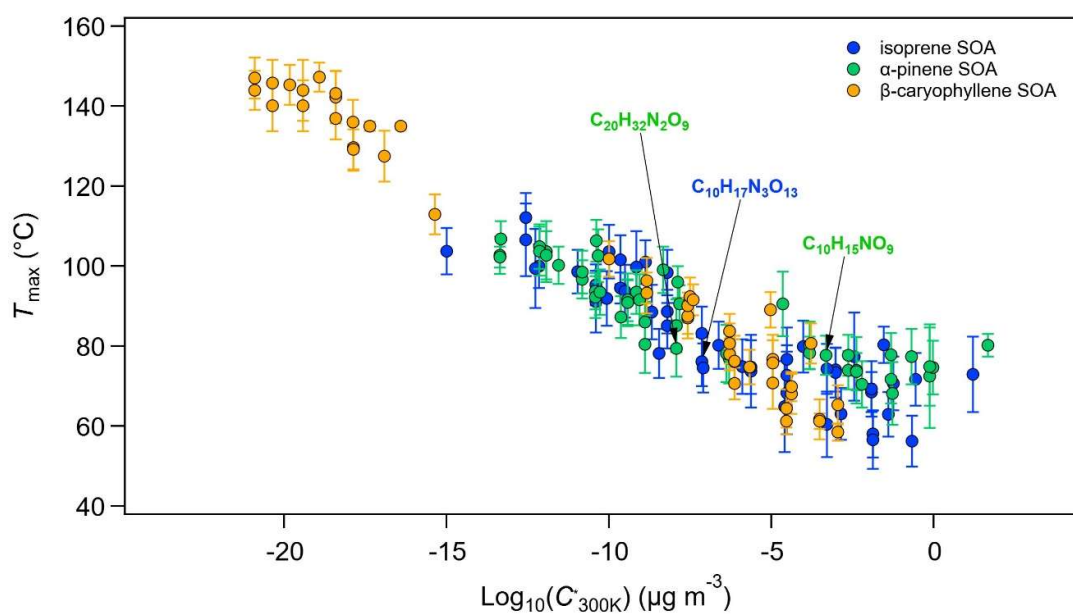
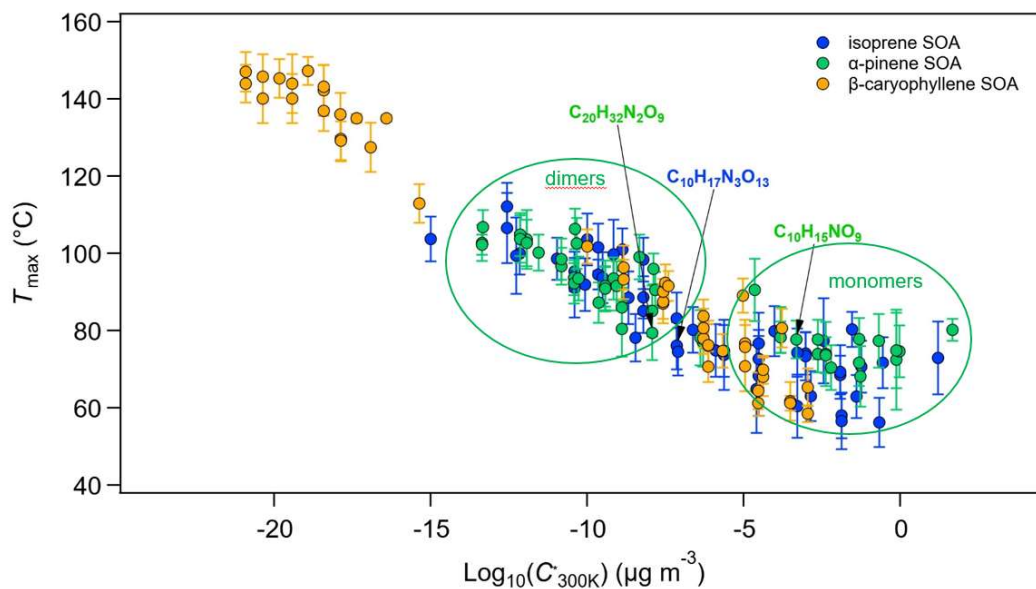


Fig. S129 Average T_{\max} from all filter samples during dark aging and photolysis versus saturation concentration $\log_{10}C^*$ by Mohr et al. (2019) of top 50 compounds from the isoprene, α -pinene SOA and β -caryophyllene SOA. Green circles indicating regions dominated by the monomers and dimers of α -pinene SOA are added to guide the eye.

SI References

- Bohren, C. F., and Huffman, D. R.: Appendix a: Homogeneous sphere, Absorption and scattering of light by small particles, Wiley-VCH Verlag GmbH, 477482, 1998.
- Buchholz, A., Ylisirniö, A., Huang, W., Mohr, C., Canagaratna, M., Worsnop, D. R., Schobesberger, S., and Virtanen, A.: Deconvolution of FIGAERO–CIMS thermal desorption profiles using positive matrix factorisation to identify chemical and physical processes during particle evaporation, *Atmos. Chem. Phys.*, 20, 7693-7716, 10.5194/acp-20-7693-2020, 2020.
- D'Ambro, E. L., Schobesberger, S., Gaston, C. J., Lopez-Hilfiker, F. D., Lee, B. H., Liu, J., Zelenyuk, A., Bell, D., Cappa, C. D., Helgestad, T., Li, Z., Guenther, A., Wang, J., Wise, M., Caylor, R., Surratt, J. D., Riedel, T., Hyttinen, N., Salo, V. T., Hasan, G., Kurtén, T., Shilling, J. E., and Thornton, J. A.: Chamber-based insights into the factors controlling epoxydiol (IEPOX) secondary organic aerosol (SOA) yield, composition, and volatility, *Atmos. Chem. Phys.*, 19, 11253-11265, 10.5194/acp-19-11253-2019, 2019.
- He, Q., Tomaz, S., Li, C., Zhu, M., Meidan, D., Riva, M., Laskin, A., Brown, S. S., George, C., Wang, X., and Rudich, Y.: Optical Properties of Secondary Organic Aerosol Produced by Nitrate Radical Oxidation of Biogenic Volatile Organic Compounds, *Environmental Science & Technology*, 55, 2878-2889, 10.1021/acs.est.0c06838, 2021.
- Huang, W., Saathoff, H., Shen, X., Ramisetty, R., Leisner, T., and Mohr, C.: Chemical Characterization of Highly Functionalized Organonitrates Contributing to Night-Time Organic Aerosol Mass Loadings and Particle Growth, *Environ Sci Technol*, 53, 1165-1174, 10.1021/acs.est.8b05826, 2019.
- Isaacman-VanWertz, G., and Aumont, B.: Impact of organic molecular structure on the estimation of atmospherically relevant physicochemical parameters, *Atmos. Chem. Phys.*, 21, 6541-6563, 10.5194/acp-21-6541-2021, 2021.
- Li, Y., Pöschl, U., and Shiraiwa, M.: Molecular corridors and parameterizations of volatility in the chemical evolution of organic aerosols, *Atmos. Chem. Phys.*, 16, 3327-3344, 10.5194/acp-16-3327-2016, 2016.
- Lopez-Hilfiker, F. D., Mohr, C., Ehn, M., Rubach, F., Kleist, E., Wildt, J., Mentel, T. F., Carrasquillo, A. J., Daumit, K. E., Hunter, J. F., Kroll, J. H., Worsnop, D. R., and Thornton, J. A.: Phase partitioning and volatility of secondary organic aerosol components formed from α -pinene ozonolysis and OH oxidation: the importance of accretion products and other low volatility compounds, *Atmos. Chem. Phys.*, 15, 7765-7776, 10.5194/acp-15-7765-2015, 2015.
- Lopez-Hilfiker, F. D., Mohr, C., D'Ambro, E. L., Lutz, A., Riedel, T. P., Gaston, C. J., Iyer, S., Zhang, Z., Gold, A., Surratt, J. D., Lee, B. H., Kurten, T., Hu, W. W., Jimenez, J., Hallquist, M., and Thornton, J. A.: Molecular Composition and Volatility of Organic Aerosol in the Southeastern U.S.: Implications for IEPOX Derived SOA, *Environmental Science & Technology*, 50, 2200-2209, 10.1021/acs.est.5b04769, 2016.
- Mohr, C., Thornton, J. A., Heitto, A., Lopez-Hilfiker, F. D., Lutz, A., Riipinen, I., Hong, J., Donahue, N. M., Hallquist, M., Petäjä, T., Kulmala, M., and Yli-Juuti, T.: Molecular identification of organic vapors driving atmospheric nanoparticle growth, *Nature Communications*, 10, 4442, 10.1038/s41467-019-12473-2, 2019.
- Nakayama, T., Sato, K., Tsuge, M., Imamura, T., and Matsumi, Y.: Complex refractive index of secondary organic aerosol generated from isoprene/NO_x photooxidation in the presence and absence of SO₂, *Journal of Geophysical Research: Atmospheres*, 120, 7777-7787, <https://doi.org/10.1002/2015JD023522>, 2015.
- Peräkylä, O., Riva, M., Heikkinen, L., Quéléver, L., Roldin, P., and Ehn, M.: Experimental investigation into the volatilities of highly oxygenated organic molecules (HOMs), *Atmos. Chem. Phys.*, 20, 649-669, 10.5194/acp-20-649-2020, 2020.
- Stark, H., Yatavelli, R. L. N., Thompson, S. L., Kang, H., Krechmer, J. E., Kimmel, J. R., Palm, B. B., Hu, W., Hayes, P. L., Day, D. A., Campuzano-Jost, P., Canagaratna, M. R., Jayne, J. T., Worsnop, D. R., and Jimenez, J. L.: Impact of Thermal Decomposition on Thermal Desorption Instruments: Advantage of Thermogram Analysis for Quantifying Volatility Distributions of

Organic Species, Environmental Science & Technology, 51, 8491-8500, 10.1021/acs.est.7b00160, 2017.